PALACKÝ UNIVERSITY OLOMOUC

FACULTY OF SCIENCE

DEPARTMENT OF PHYSICAL CHEMISTRY

Nanostructured photoanodes based on metal oxides for photoelectrochemical water splitting

Diploma Thesis

Author: Bc. Vojtěch Šarafín

Subject of study: Material Chemistry

Form of study: Full-time

Supervisor: Ing. Štěpán Kment, Ph.D.

Olomouc 2018

Declaration

I declare that I worked independently on my diploma thesis under guidance of Ing. Štěpán Kment, Ph.D. and all used sources are included in bibliography.

Olomouc …….

…….
Handwritten signature

Acknowledgement

I would like to thank my supervisor Ing. Štěpán Kment, Ph.D. for his leadership, advices, patience and opportunity to work on such an interesting topic. I would also like to thank Ing. Hana Kmentová, Ph.D. for her practical advices in laboratory and for her kindness.

Then, it is really important to thank the people who helped me with physical characterization, electrochemical measurements and with interpretation of results:

- Rambabu Yalavarthi, Ph.D. - Electrochemical impedance spectroscopy
- Mgr. Josef Kašlík - X-ray diffraction
- Mgr. Dominik Janáček - Scanning electron microscopy and EDS spectra
- Sergii Kalytchuk, Ph.D. - Absorbance spectra
- Mgr. Martin Petr - X-ray photoelectron spectroscopy
- RNDr. Václav Ranc, Ph.D. - Raman spectroscopy

Speciální poděkování patří mé rodině za nekonečnou trpělivost, pochopení a podporu nejen po dobu psaní této práce, ale po celou dobu studia.

V neposlední řade bych velmi rád poděkoval mým spolužákům a přátelům za pomoc a povzbuzování. Chtěl bych také poděkovat klukům z kapely No Doe za trpělivost a respektování mých časových možností v průběhu psaní této diplomové práce.

Nakonec patří velké díky mé přítelkyni Veronice Tabákové, bez které bych tuto práci nikdy nenapsal.

Bibliographical identification

Authors first name and surname:	Vojtěch Šarafín
Title:	Nanostructured photoanodes based on metal oxides for photoelectrochemical water splitting
Department:	Department of Physical Chemistry
Type of thesis:	Master
Supervisor:	Ing. Štěpán Kment, Ph.D.
The year of presentation:	2018

Abstract: Present environmental works are still increasingly important due to climate change directly related to energy crisis. Solution of this crisis could be in replacing fossil fuels by a sustainable and renewable energy source as e.g. hydrogen. However, most of hydrogen is still produced from natural gas by steam reforming, which does not solve the environmental issue. That is why new pathways of the hydrogen production are still intensively sought. One of the most promising solution is based on a sun-driven photoelectrochemical (PEC) water splitting. This diploma thesis is focused on the preparation, characterization and testing the photoactive materials that are applied as photoelectrodes in the PEC cells. As the photoanode materials titanium dioxide (TiO_2), tungsten trioxide (WO_3) and bismuth

vanadate ($BiVO_4$) were investigated. These materials were prepared by various methods including hydrothermal method, drop casting and electrodeposition. Particular attention was devoted to $BiVO_4$ due to its promising properties such as wide absorption range and high photoactivity. Moreover, $BiVO_4$ properties were improved by Mo and W doping. The structural properties of the materials were studied by several techniques which included scanning electron microscopy (SEM), X-ray diffraction (XRD), Raman spectroscopy, UV/VIS spectroscopy or X-ray photon spectroscopy (XPS). The photoelectrochemical properties were studied by linear sweep voltammetry (LSV), chronoamperometry (ChAM) and electrochemical impedance spectroscopy (EIS). The results of this diploma thesis prove that $BiVO_4$ has a potential to be used in artificial photosynthetic devices.

Key words: sun-driven water splitting, hydrogen, photoelectrochemistry, bismuth vanadate, titanium dioxide, tungsten trioxide, metal doping

Number of pages: 73

Language: English

Bibliografické údaje

Jméno a příjmení autora:	Vojtěch Šarafín
Název práce:	Nanostrukturované fotoelektrody na bázi kovových oxidů pro fotoelektrochemické štěpení vody
Typ práce:	Magisterská
Pracoviště:	Katedra fyzikální chemie
Vedoucí práce:	Ing. Štěpán Kment, Ph.D.
Rok obhajoby:	2018
Abstrakt:	Současné enviromentální studie jsou stále více důležité kvůli klimatickým změnám úzce souvisejících s energetickou krizí. Řešením této krize může být nahrazení fosilních paliv udržitelnými a obnovitelnými zdroji energie jako je například vodík. Většina vodíku je ovšem stále vyráběna parní reformací zemního plynu, což neřeší environmentální problémy. Proto jsou hledány nové způsoby ekonomické a environmentálně příznivé produkce vodíku. Jedno z nejslibnějších řešení je založeno na solárním fotoelektrochemickém (PEC) štěpení vody. Tato diplomová práce se zabývá přípravou, charakterizací a testováním fotoaktivních materiálů, které jsou používány jako fotoelektrody v PEC celách. Oxid titaničitý (TiO_2), oxid wolframový (WO_3) a vanadičnan bismutitý

($BiVO_4$) byly zkoumány jakožto materiály pro výrobu fotoanod. Tyto materiály byly připraveny různými metodami jako je například hydrotermální metoda, metoda drop casting anebo elektrodepozice. Zvláštní pozornost byla věnována $BiVO_4$ vzhledem k jeho slibným vlastnostem jako je například absorpce ve viditelné oblasti spektra a značná fotoaktivita. Navíc byly vlastnosti $BiVO_4$ vylepšeny dopováním Mo a W. Strukturální vlastnosti připravených materiálů byly studovány technikami, které zahrnovaly elektronovou skenovací mikroskopii (SEM), rentgenovou difrakci (XRD), Ramanovu spektroskopii, UV/VIS spektroskopii nebo fotoelektronovou spektroskopií (XPS). Fotoelekrochemické vlastnosti byly studovány lineární voltametrií (LSV), chronoamperometrií (ChAM) a elektrochemickou impedanční spektroskopií (EIS). Výsledky této diplomové práce potvrzují, že $BiVO_4$ může být potenciálně využit zařízeních na tzv. umělou fotosyntézu.

Klíčová slova: Přímé solární štěpení vody, vodík, fotoelektrochemie, vanadičnan bismutitý, oxid titaničitý, oxid wolframový, dopování kovy

Počet stran: 73

Jazyk: Anglický

Table of contents

1 Introduction

According to the United Nations[1], in 2050 on planet Earth will be 9.5 billion people and in 2100 there can be almost 11 billion people. That is one of the reasons why there will be huge demand for water, food and basic human needs, which apparently cannot be fulfilled without clean and renewable energy sources.

There are no doubts about negative effects of combustion of fossil fuels, currently still the main energy sources, on the environment and consequently on human health[2]. There are many possibilities how to get clean and environment-friendly energy. The well-known and already used ones are devices using nature renewable sources such as sun, water, wind, thermal drills or biomass. They all have their advantages and disadvantages. However, the storage and transport of these alternative sources of energy still represents the major challenges. The modern batteries are still too big and heavy and despite that their energy density continuously increases another ways how to make and store clean energy are still widely studied[3,4,5].

One of the most promising sources of such clean and renewable energy is hydrogen (H_2). Hydrogen can be converted into energy through fuel cell. This device need only oxygen and hydrogen to make electric energy. Oxygen is everywhere around us and there is no problem with its gathering, but hydrogen is difficult to produce. We can obtain the purest hydrogen by the electrolysis of water, but this process is energetically more demanding than the energy output achieved by its subsequent exploiting, which is obviously economically ineffective. Another nowadays hydrogen technology is steam reforming from hydrocarbons. This process is the most used one. But it still needs hydrocarbons like methane which can be used also as fuel and, moreover, it is another considerably source of CO_2, which causes greenhouse effect.

$$CH_4 + H_2O \rightarrow 3H_2 + CO_2$$

With respect to all aforementioned arguments, there is desperate need of cheap, clean and no-waste hydrogen production process. In this work I focus on the preparation of nanostructured photoanodes, which are used in photoelectrochemical cells (PEC). The PEC cells currently represent one of the most promising devices for producing hydrogen in economically viable manner using the process known as photoelectrochemical water

splitting. This process needs only small amount of applied voltage, sun light and water. The details of this process will be described and discussed on next pages of this work.

THEORETICAL PART

2 Photoelectrochemistry

For direct water splitting process is required 237.2 kJ/ mol. Under standard condition, this energy can split H_2O into H_2 and ½ O_2. With respect to Nernst equation (equation 1.1), one can calculate required potential of water splitting reaction.

$$E_{red} = E^0_{red} - \frac{RT}{zF} \ln \frac{a_{red}}{a_{ox}} \qquad (1.1)$$

Where E_{red} is the half-cell reduction potential, E^0_{red} is the standard half-cell reduction potential, R is the universal gas constant ($R= 8.314\ J{\cdot}K^{-1}$), T is the thermodynamic temperature in kelvins, F is the Faraday constant ($F = 96\,485\ C{\cdot}mol^{-1}$), z is the number of transferred electrons and a is the chemical activity. So, the energy 237.2 kJ/ mol corresponds to E^0= 1.23 V per electron. In our case, we want to use solar energy and the value of 1.23 eV leads us to the wavelengths of radiant light, which our semiconductor must absorb. Equation which connects energy, wavelength and frequency of photon is called Planck´s equation (equitation 1.2).

$$E = h\nu = \frac{hc}{\lambda} \qquad (1.2)$$

Where h is Planck´s constant ($h = 6.626 \cdot 10^{-34}\ J{\cdot}s$), c is speed of light ($c= 3.00 \cdot 10^{8}\ m{\cdot}s^{-1}$), ν represents frequency and λ is wavelength. Wavelength of photons absorbed in water splitting material must be equal or shorter than 1000 nm.

2.1 Photoelectrochemical cells

Photoelectrochemical (PEC) cells are devices used for sunlight to electricity conversion or sunlight to chemical fuel conversion. Therefore, we distinguish two types of cells. First type is a regenerative cell (Figure 1 a), which converts sunlight to electric energy and leaves no chemical changes. Photons must provide sufficient amount of energy that will generate electron-hole pairs, which are then separate by an electric field. Negative charges move through the material and are collected into external circuit. On the other hand, holes carry positive charge and they are absorbed on the surface of material by reduced form of

molecule, which is then transformed into oxidized form and finally is reduced by electrons that comes back to cell from external circuit.

Second type of PEC cell is the photosynthetic cell (Figure 1 b). There are few differences compare to regenerative cell. Electron and holes react with two redox systems. Electrons react with one system at the counter electrode and holes react with the second system at the surface of bulk material. For example, water splitting is realized by electrons which reduce hydrogen at cathode and by holes which oxidize oxygen at anode[6].

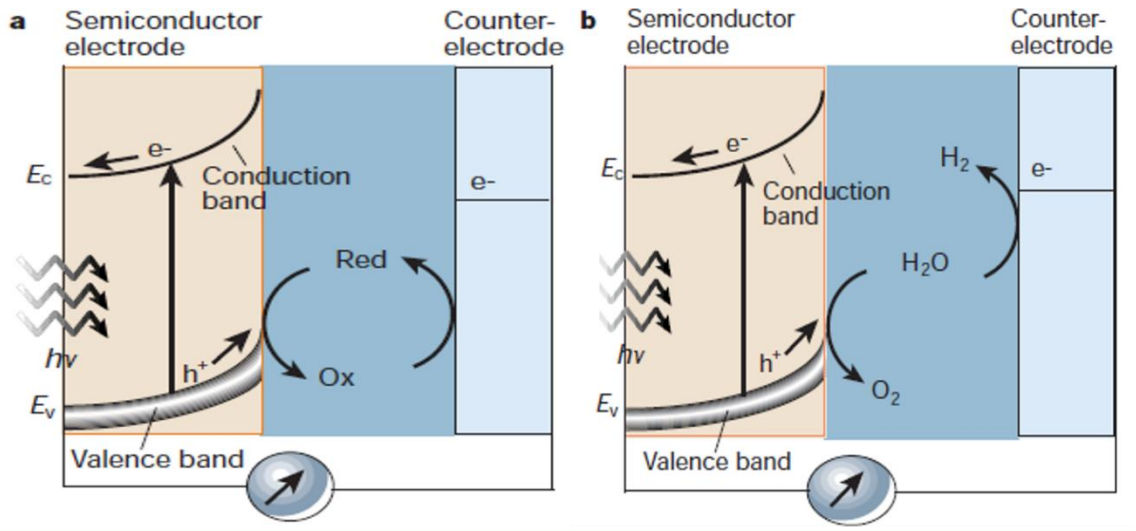

Figure 1- Principle of photoelectrochemical cells a) regenerative cell b) photosynthetic cell (Grätzel, M. Photoelectrochemical cells. Nature 414, 338–344 (2001))

Mostly used materials as photoelectrode are n-type (photoanode) and p-type(photocathode) semiconductors[7,8].

2.2 Semiconductors

One of the most important attribute of semiconductor is the band gap energy E_g. This energy represents difference between top of valence band and bottom of conductive band in semiconductors electronic band structure. Generally, according to band gap energy we can distinguish semiconductors, insulators and conductors. In conductor´s electronic band structure, there is no band gap and the valence and conductive bands are overlapped. On the other hand, insulators have the band gap energy larger than 9 eV, because for such energy, the ambient temperature 300K do not provides enough thermal energy for

electron transfer from valence band to conductive band. Between insulators and conductors lie semiconductors, which have got their bang gap smaller than insulators. It means that electrons in valence band can be promoted to conduction band. Comparison of insulators, semiconductors and conductors is shown in Figure 2.

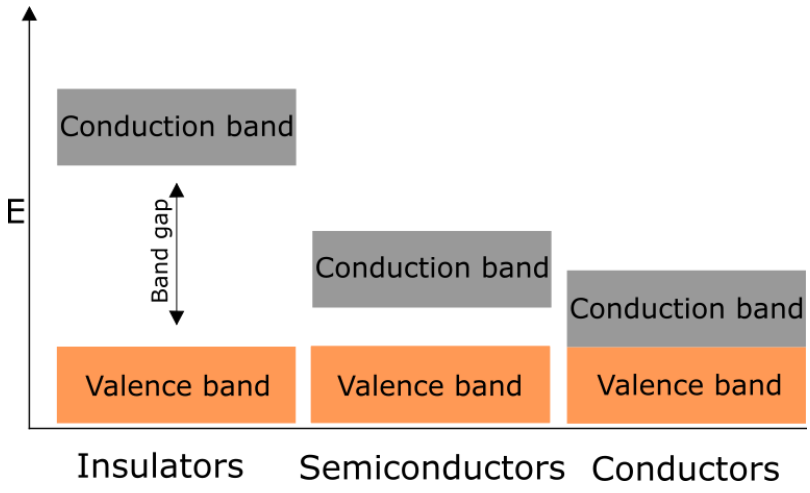

Figure 2 – Diagram of electronic structure of insulators, semiconductors and conductors

The occupation of each band can be approximated by the Boltzmann function (equation 1.3).

$$n \approx N_0 \exp\left(-\frac{E_0 - E_F}{kT}\right) \qquad (1.3)$$

Where n is electron occupancy, N_0 is number of particles at ground state at absolute zero, E_0 is ground state energy, E_F is Fermi level and k is Boltzmann constant (k = $1.38 \cdot 10^{-23}$ $m^2 \cdot kg \cdot s^{-2} \cdot K^{-1}$). Fermi level is defined at absolute zero as the energy of the topmost filled orbital or as an energy at which probability of finding electron is ½ [9,10].

2.2.1 Types of semiconductors

Semiconductors properties can be modified by doping techniques. These operations insert into crystalline structure impurities which generate more conductive electrons or holes. Addition of impurities such as phosphorus or aluminium into the silicon structure shifts Fermi level further or closer to the valence band. Based on this knowledge we distinguish

three basic types of semiconductors: undoped, n-type and p-type (Figure 3). In undoped, i.e. the intrinsic semiconductor the Fermi level is in the middle of band gap. N-type semiconductors produces more negative charges (electrons) by adding element with more valence electrons than semiconductor structure contains. In this case, Fermi level is shifted closer to conductive band. On the other hand, p-type semiconductors have got in their structure elements with less valence electrons than theirs lattice contains and that is why p-type semiconductors produce positive charges (holes). So, Fermi level is shifted closer to the valence band.

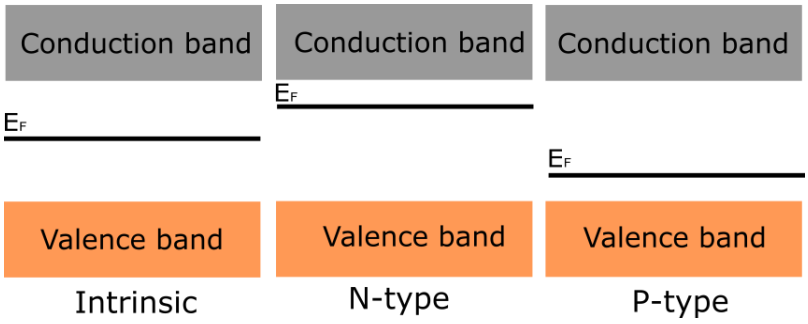

Figure 3 – Three basic types of semiconductors

2.3 Semiconductor – electrolyte interface

If semiconductor is placed into an electrolyte, which contains redox couple bearing chemical potential, electrons start moving across electrode and electrolyte junction until an equilibrium is reached. As the equilibrium, in this case, is meant equalization of Fermi level and electrochemical potential (Nernst potential). The flow of electron produces on both sides of equilibrium regions a different charge distribution which depend on bulk material. This phenomenon is known as the space – charge layer. At electrolyte region, this corresponds to the Helmholtz and Gouy – Chapman layer, well-known as the electrolytic double layer (compact and diffuse layer). On the semiconductor side of the equilibrium, the band banding is formed due to contact with electrolyte. The band bending depends on the Fermi level of bulk material. If the Fermi level and flat band potential are equals, there is no charge transfer on both sides of equilibrium and bands are flat. When semiconductor side obtains more electrons, one creates an accumulation layer. On the other hand, if electrons move from solid phase into liquid phase, a depletion layer is formed and consequently the positive excess holes are created. However, in some cases,

depletion of electron can reach intrinsic level and then we can observe p-type semiconductor at the surface and n-type in the bulk. This phenomenon is known as an inversion layer[11,6,12,13]. Figure 4 further describes behaviour of electronic energy levels at the semiconductor/ liquid interface.

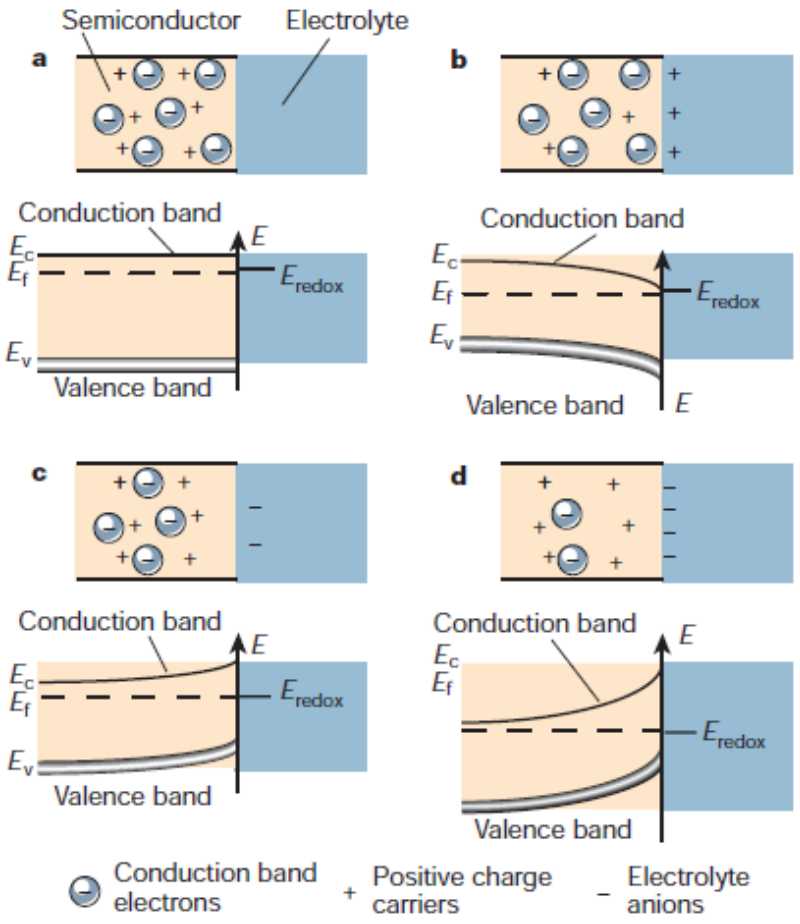

Figure 4 - Electronic energy levels at the interface semiconductor/ liquid. ***a)*** *flat band potential and Fermi level are equal with no space – charge layer* ***b)*** *accumulation layer, where is more electrons in solid phase producing band bending towards the interface* ***c)*** *depletion layer, where is more electrons in liquid phase and as consequence is upward band bending* ***d)*** *inversion layer, semiconductor is p-type on the surface and n-type at the bulk. (Grätzel, M. Photoelectrochemical cells. Nature 414****,*** *338–344 (2001))*

2.3.1 Flat band potential

Very important property of every semiconductor material in photoelectrochemistry is the flat band potential. The flat band potential is used as a tool for determining of energetic levels of valence and conductive band edges of semiconductors when they are in the contact with electrolyte and under certain applied voltage. It can be obtained by

measuring the capacity of semiconductor – electrolyte junction. The semiconductor is exposed to the voltage, which increases the potential step across the junction and the differential capacity is calculated as a function of the applied potential. In a depletion space only, the charge capacity state can be measured, because the Helmholtz layer capacity is bigger than the space charge capacity. This condition is followed by the applied bias voltage according to the Mott – Schottky equation (equation 1.4):

$$\frac{1}{C_{SC}^2} = \frac{2\left(\frac{\Delta\Phi_{SC}RT}{F}\right)}{\varepsilon_0 \varepsilon N} \qquad (1.4)$$

Where $\Delta\Phi_{SC} = V - V_{FB}$ represents the voltage drop in the space - charge layer, ε is dielectric constant of semiconductor, ε_0 is permittivity of vacuum ($\varepsilon_0 = 8.854 \cdot 10^{-12}$ F/m) and N represents ionized donor dopant concentration. The plot of square reciprocal capacity against the applied voltage gives a straight line and this is extrapolated to $1/(C_{SC})^2 = 0$ to derive the flat band potential[14,6].

2.4 Solar - to - chemical energy conversion efficiency

Most of the energy sources on the Earth originally comes from the Sun. In nature, the sun-to-chemical energy conversion is well known. Living organisms are not able to convert directly light in-to energy and that is why they developed the process called photosynthesis producing glucose. This process achieves efficiency around 25% under full irradiation[15]. In our case, the direct water splitting provides a hydrogen as the energy source. The most important properties of semiconductors that determine the overall efficiency of the water splitting are wide sun light absorption, high charge separation efficiency and high driving forces for the redox electrochemical reactions resulting from appropriate band energy levels. The theoretical maximum conversion efficiency is 83% which is much more than a steam engine or combustion engine[16]. To gain a real process efficiency, these measurements can be done in two – electrode configuration experiment. Efficiency calculations can be done based on photocurrent density (J) – applied voltage (V) measurements with respect to equation 1.5.

$$\eta = \frac{J_{mp}(1.23V - V_{app})}{P_{in}} \qquad (1.5)$$

Where J_{mp} is externally measured photocurrent density, V_{app} is applied voltage measured between the photoanode and photocathode and P_{in} is power density of illumination.

Calculations of solar conversion efficiency for photoanode or photocathode separately can be done by using data from three-electrode cell measurements during illumination. It is important to know efficiency of photoelectrodes at both sides of reactions separately, because of improving their properties. Equation 1.6 describes how to calculate photoelectrode efficiency.

$$\eta = \frac{J_{mp}\, V_{mp}}{P_{in}} \qquad (1.6)$$

Where J_{mp} is current density at maximum power point, V_{mp} is the voltage at the maximum power point. These two quantities are connected by the relation $P_{PA} = \mathrm{J}_{mp} \cdot V_{mp}$. This calculation is identical to a photovoltaic cell efficiency calculation. Nevertheless, when the potentiostat works with three electrodes arrangement, polarization losses associated with driving the reaction at the counter electrode is not taken in overall result of water splitting reaction[10].

3 Materials used for direct water splitting

As was mentioned before, there are two types of photoelectrodes used for direct sun-driven water splitting – photoanodes and photocathodes. In this work the photoanode materials will be exclusively subscribed. Photoanodes evolving oxygen can only be an n-type semiconductor, so the electric field generated by band bending will attract holes to the surface, which then oxidize water. Band gap have to be relatively small for visible light absorption and edges of valence and conductive bands must correspond to oxygen evolution reaction (OER) potential. Additionally, photoanode have to be stable in harsh electrolytes (usually highly acidic or basic solutions) and under irradiation (i.e. stable against photocorrosion). There are many suitable materials and few of them will be described in more details[17].

3.1 Titanium dioxide

One of the most explored materials used for sun-to-energy conversion is titanium dioxide (TiO_2). Its suitability for water photolysis was discovered by Akira Fujishima and Kenichi Honda at 1972[18]. Since the release of this paper, TiO_2 was widely used for photocatalysis of pollutants[19,20], photocatalytic carbon dioxide reduction into the energy fuels[21,22] , solar cells[23,24], supercapacitors[25] or Li – ion batteries[26].

TiO_2 naturally exists in three crystalline structures such as anatase, rutile and brookite (Figure 5). All three polymorphs contain titanium cations which are six-fold coordinated to oxygen anions. Titanium and oxygen atoms create together distorted TiO_6 octahedra. These octahedrons are arranged in different crystal lattices such as tetragonal for anatase and rutile and orthorhombic for brookite[27]. Among polymorphs, rutile is considered as the most stable bulk phase, but at the nanoscale anatase and brookite are more stable than rutile, because of lower surface energy[28].

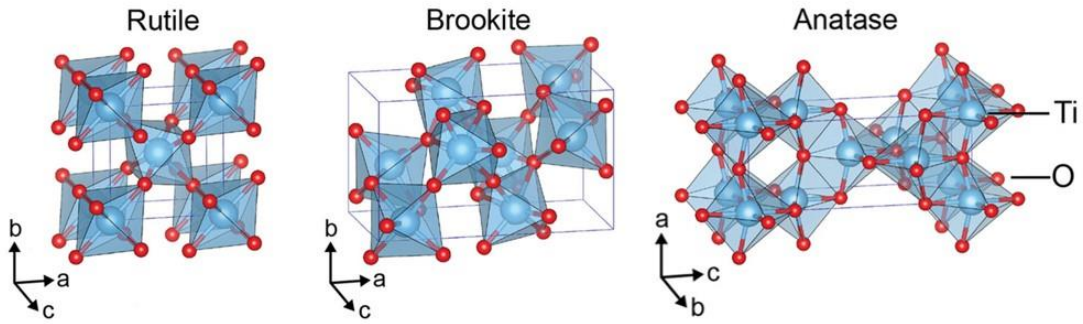

Figure 5 - Three natural crystalline phases of TiO_2. (Haggerty, J.E.S. High-fraction brookite films from amorphous precursors. Scientific reports 7, 15232 (2017))

The growth of TiO_2 crystal structures is affected by many factors such as pH, annealing temperature or synthesis method. For example, TiO_2 nanorods, prepared by hydrothermal method using peroxide titanic acid solutions with different pH values, were composed only of rutile phase, when pH was lower than 8. At pH 8 – 10, rutile and brookite phases were present in the samples. However, when pH increased up to 10, only anatase phase was found[29].

Annealing temperature is very important factor in the preparation process of all photoactive semiconductors in general. In case of TiO_2 some important findings regarding

the thermal treatment have been reported. Alsawat et al. performed experiments with TiO_2 nanotubes which were annealed at 250 °C, 450 °C, 650 °C and 850 °C. Before annealing, only amorphous phase was observed. Anatase phase appeared around 250 °C and relative intensity of anatase XRD pattern increased till 650 °C. At this point, a mixture of rutile and anatase (13.5 % and 86.5%) was observed, which showed the best PEC properties. Up to 650 °C, PEC properties declined due to anatase phase decreasing while rutile peak increased[30]. Annealing above 700 °C transformed all polymorphs to rutile[31]. Among other polymorphs, anatase provides the best photocatalytic performance, but the mixture of anatase and rutile shows better activity than a pure anatase crystal[32]. This fact is cause by synergistic effect of smaller band gap energy of rutile (3.0 eV) and due to more negative position of conduction band of anatase compared to rutile conduction band[33,34].

Apparently, the synthesis methods also play significant role for TiO_2 final structure. As was mentioned before, hydrothermal method is a very common way how to prepare TiO_2 nanorods (one dimensional structures). It requires stainless steel vessel due to high pressure and temperature during preparation[35,36]. Solvothermal method is very similar to the hydrothermal. However, solvothermal method mostly uses organic solvents while hydrothermal method uses water [37,38]. Both methods include TiO_2 nanoparticles, $TiCl_4$ or tetrabutyl titanate as precursors. Besides these methods, there are many others such as electrochemical anodization[39], chemical vapour deposition[40], electrospinning[41] or magnetron sputtering[42].

Despite of all advantages of TiO_2 such as simple preparation and high stability, TiO_2 suffers from wide band gap and fast recombination of hole – electrons pairs. Wide band gap causes absorption merely in UV region and UV rays account only 6% of Earths sunlight[43]. These disadvantages could be improved via doping techniques[44], heterojunction with other phases[45], enlargement of specific surface area[46] or connection with nanoparticles[47].

3.2 Tungsten trioxide

Tungsten trioxide (WO_3) is another multifunctional photosensitive material. Butler et al. published water splitting properties of WO_3 at 1976[48]. Besides water splitting, WO_3 found applications in dye-sensitized solar cells[49], heterogenous catalysis[50] or superconductivity[51].

Several crystal phases of WO_3 are known (triclinic, monoclinic, orthorhombic, tetragonal, hexagonal, cubic). The group of triclinic, tetragonal, monoclinic, orthorhombic phases create almost same chessboard-like structure made of WO_6 octahedrons and they can transform into each other. Thus, WO_3 have only three different structures – chessboard-like, hexagonal and cubic. Chessboard-like (mostly called γ-WO_3 or just monoclinic) was reported as the photoactive one[52].

There are several factors that affect structural properties of WO_3. Annealing temperature is one of them. According to the XRD studies, orthorhombic $WO_3 \cdot 0.33\ H_2O$ nanorods are transformed to the hexagonal structures by annealing at 400 °C and above 500 °C are converted to the monoclinic form[53]. Dimensional structure can be also controlled. For example, one-dimensional structure is achieved by electro-spinning techniques. The fabrication of WO_3 nanofibers are prepared by electro-spinning of polyvinyl pyrrolidone, citric acid and tungsten acid as precursors. These fibers display good mechanical properties with high surface-to-volume ratio[54]. Two-dimensional structures such as nanosheets are prepared for instance by a solid-liquid phase arc discharge route in aqueous environment. These nanosheets are used for photocatalytic reduction of carbon dioxide into hydrocarbon fuels[55]. And finally, three-dimensional structure is observed by using various template assisted methods. For example, this method can use colloidal crystals template of poly (methyl methacrylate) spheres and in their presence, WO_3 grow in nanoparticles among the empty spaces of poly (methyl methacrylate) spheres. Final material shows porous structure and could be used in photocatalysis[56]. Besides these methods, there are more other ways how to prepare WO_3 such as electrochemical anodization[57], sol-gel method[58] or hydrothermal method[59].

The main obstacles in the use of WO_3 as the photoanode are quick electron-hole recombination and the fact that conductive band level is relatively more negative than the

potential of oxygen reduction[60]. Also, there are known techniques that can improve photocatalytic properties. For example, graphene/WO_3 composite shows two times higher photocurrent density than pure WO_3 due to enhanced visible light absorption and reducing the charge carriers recombinations[61]. Another way how to improve photocatalytic properties is noble metal deposition[62] or by alkali hydroxide loading[63].

3.3 Bismuth vanadate

The attention has been paid to bismuth vanadate ($BiVO_4$) since 1963, when was firstly prepared by Roth and Waring[64]. However, the photoactivity of $BiVO_4$ was discovered after 35 years in 1998 by Kudo et al. For the first time, they observed oxygen evolution reaction under light irradiation by using a $BiVO_4$ powder[65]. It is highly promising material for direct water splitting applications due to relatively small band gap (2.4 eV) and because the conduction band edge energy of $BiVO_4$ is almost same as the hydrogen evolution potential. This supports the desired cathodic photocurrent onset and higher photocurrent performance at lower potentials than other photoanodes[66]. The $BiVO_4$ theoretical solar-to-hydrogen efficiency reaches 9.2% with the highest photocurrent of 7.5 mA/cm^2 under AM 1.5 solar irradiation ($100mW/cm^2$)[67,68]. Figure 6 shows the comparison of the theoretical maximum performance of the four the most widely investigated metal semiconductors acting as photoanodes including TiO_2, WO_3, Fe_2O_3 and $BiVO_4$. Last but not the least, $BiVO_4$ is low a cost, stable and nontoxic material[69].

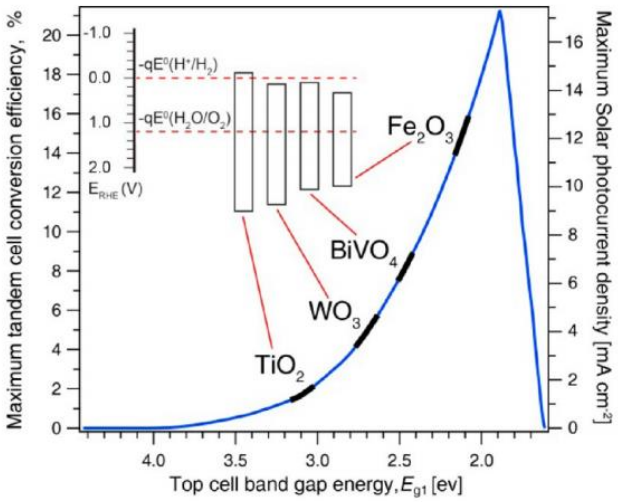

Figure 6 - $BiVO_4$ among the other materials used as a photoanodes showing maximum tandem cell conversion efficiency, maximum photocurrent density and comparison of their band gaps. (Prévot, M. S. & Sivula, K. Photoelectrochemical Tandem Cells for Solar Water Splitting. J. Phys. Chem. C 117, 17879–17893 (2013))

$BiVO_4$ exists in three different structures - tetragonal dreyerite, monoclinic clinobisvanite and orthorhombic pucherite. Only monoclinic clinobisvanite form is suitable for the sun-driven water splitting, due to $6s^2$ lone pair of Bi^{3+} that distort monoclinic $BiVO_4$ polyhedron more than in tetragonal $BiVO_4$ polyhedron[70]. An irreversible conversion from tetragonal to monoclinic form is obtained when annealing temperature is about 400-500 °C. In contrast a reversible transition between monoclinic and tetragonal structure occurs at annealing temperature of 255 °C[71]. In monoclinic scheelite-like structure (Figure 7), bismuth is coordinated to oxygen in distorted octahedron and in the centre of oxygen distorted tetrahedron is vanadium, which is in line with stoichiometry of a Bi^{3+} ($5d^{10}6s^2$), V^{5+} ($3d^{10}$) and O^{2-} ($2p^6$) electronic system[72].

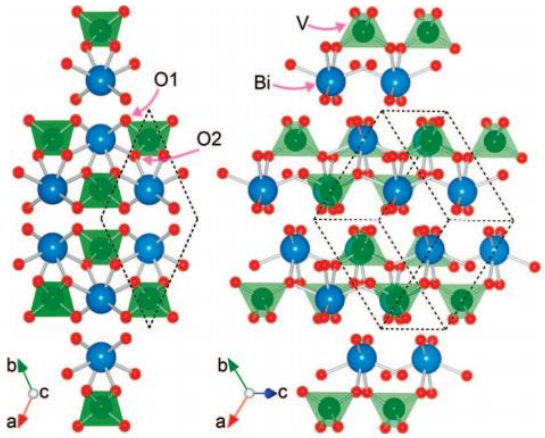

Figure 7 – $BiVO_4$ crystal structure with bismuth (blue), vanadium (green) and oxygen (red) atoms. Dotted black lines show monoclinic primitive cell. (Walsh, A., Yan, Y., Huda, M. N., Al-Jassim, M. M. & Wei, S.-H. Band Edge Electronic Structure of $BiVO_4$: Elucidating the Role of the Bi s and V d Orbitals. Chem. Mater. 21, 547–551 (2009))

One of the most common method for the preparation of $BiVO_4$ photoanode is a solution-based metal organic decomposition. This method uses chemicals containing Bi^{3+} (bismuth nitrate, bismuth-2-ethyl-hexanote) and V^{3+} or V^{5+} (vanadium acetylacetonate, vanadium-tri-isopropoxy oxide, ammonium metavanadate, vanadium chloride) ions which are dissolved in the solution and then are spread on the surface of a conductive substrate by spin coating[73], drop-casting[74] or spray pyrolysis[75]. Another approach for $BiVO_4$ fabrication is the electrochemical deposition. This typically three electrodes system contains a counter electrode, working electrode and reference electrode. All three electrodes are submerged into a solution that contains Bi^{3+} and V^{4+} ions. The Bi^{3+} ions are attached to the surface of the working electrode on which a negative potential is applied. Then V^{4+} ions are oxidized to V^{5+} due to the applied potential. These ions immediately react with Bi^{3+} and an amorphous phase of $BiVO_4$ precipitate. After this electrodeposition, samples are calcinated to give crystalline phase. Excess of V_2O_5 is then removed by washing in an alkaline solution. This procedure was described by Myung et al.[76]

$BiVO_4$ is very promising material for direct water splitting, but it also has its disadvantages. The well-known drawback is a poor charge transfer to the electrolyte and fast surface recombination of electrons and holes[77]. These limitations has been extensively addressed by various strategies including morphology control[78],

heterojunction[79] or loading of oxygen evolution catalysts[75]. Very common approach to improve the performance is doping of $BiVO_4$ lattice by various metals. Even small amount of metal can greatly influence photoelectric properties of $BiVO_4$ due to improving electrical conductivity and charge carrier density. Beside these effects, doping causes shifting of Fermi level towards to conductive band minimum and valence band maximum[80]. Most promising and most used metals are W, Mo[81] or Nb[82] because of similar ionic radius and higher valence[83].

4 Characterization techniques

For better understanding of true nature of observed phenomena, we need techniques that will help us to explain how our system works and how can we improve its properties. Therefore, several characterization techniques will be described in this part of my diploma thesis.

4.1 X-Ray Diffraction

X-ray diffraction (XRD) is an analytical non-destructive method used to determine crystal structures. This method uses part of electromagnetic radiation that was discovered by Wilhelm Conrad Röntgen in 1895 and for which he achieved the Nobel Prize in 1901. Seventeen years after Röntgen´s discovery, Max von Laue suggest that X-rays passing through the crystal could diffract, because wavelength of X-ray radiation is comparable to the distances among the atoms in crystal lattice. Diffraction of certain wavelengths is determined by the Bragg´s condition (equation 1.7):

$$n\lambda = 2d\ sin\theta \tag{1.7}$$

Where n is any integer, λ is wavelength, d is spacing between lattice planes and θ is diffraction angle[84]. Diffracted arrays are detected and counted. Output patterns are compared to standard reference patterns.

Basically, the X-ray diffractometers are composed of three main parts such as source of radiation, sample holder/manipulator and detector. The cathode ray tube is widely used as the X-ray source, where the filament is heated, and the high voltage is applied. Due to these conditions, electrons begin to hit the target. If the energy of coming electrons is high

enough to dislodge inner electrons of target material, the X-ray radiation is produced. After irradiation of sample, X-rays are collected at detectors such as scintillation counter, CCD (charged -coupled device) detector or a X-ray film, which is still used in medicine applications[85,86].

Besides the XRD, there are other X-ray techniques. For example, X-ray photoelectron spectroscopy (XPS), which analyses kinetic or binding energies of electrons emitted after the X-ray irradiation. The XPS can determine oxidation state of elements or empiric formula[87]. Furthermore, other X-ray techniques are Auger electron spectroscopy[88], which analyses double ionized electrons, or neutron diffraction, which is able of tracking magnetic properties of material[89].

4.2 Electron microscopy

Optical microscopes allow us to see objects with resolution of only 200 nm due to diffraction limit, which is described by Abbe´s equation (1.8):

$$d = \frac{0.612\,\lambda}{n\,sin\alpha} \qquad (1.8)$$

Where d is resolution, λ is wavelength of imaging radiation, n is refraction index of medium between lens and source, α represents half angle of the cone of light from sample accepted by objective[90]. Diffraction limit of optical microscope is about half of wavelength of the visible light used. Electron microscopes use electrons instead of photons. Wavelength of electron beam is much lower (for common voltage 10kV is λ=0.012 nm). Accordingly, theoretical resolution of electron microscope is five orders of magnitude better compared to optical microscope. Unfortunately, real resolution of electron microscope is only 2 - 3 orders of magnitude better compared to optical microscope, but it still allows us to see atoms and nanostructures[91].

Electron microscopy is divided in two basic construction streams. Transmission electron microscopy (TEM) allows electrons to fly through the sample and the final image is proceed on fluorescent screen. This type of electron microscope allows to see structure of illuminated specimens. On the other hand, scanning electron microscope (SEM) is better for imaging surface of specimen due to electrons reacting with the surface of

specimen. Electrons are losing energy and are reflected to the detector. So, the secondary electrons create detailed image of specimen surface compared to the TEM.

Both microscopes consist of similar parts such as an electron gun. Electron gun thermionically emits electron beam that is modified by electromagnetic coils. The most used electron guns are Schottky source, tungsten filament or lanthanum hexaborite tip. Electromagnetic coils serve mainly as a condenser lens. Different arrangement of optical microscope, SEM and TEM is described at Figure 8.

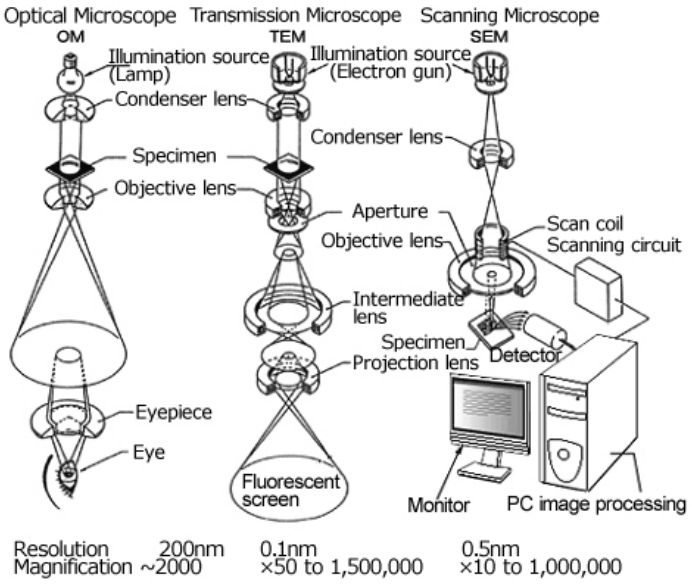

Figure 8 - Comparison of optical microscope, SEM and TEM (Scanning Electron Microscopes (SEM) | Introduction to JEOL Products | JEOL Ltd.)

Besides secondary electrons, also X-rays, cathodoluminescence or Auger electrons are emitted from the illuminated spot. These energies carry an information and can be analysed by energy dispersive spectrometer (EDS) or wavelength dispersive spectrometer (WDS). Both spectrometers use X-ray radiation for analysis, but EDS analyse energy of photons while WDS analyse photons wavelength. EDS is more common due to lower price and faster spectrum acquisition. All things considered, an output of EDS measurement is a spectrum, which is compared to standard reference spectrum, and can confirm presence of elements[92,91].

4.3 UV-VIS spectroscopy

While XRD and SEM analyse a high energy radiation, UV/VIS spectroscopy analyses ultraviolet (UV) and visible (VIS) radiation that are less energetic. UV and VIS radiations are part of electromagnetic spectrum with wavelength around 100 - 420 nm for UV and 420 - 700 nm for VIS. Photons of these radiations have enough energy to excite electrons from their basic energy levels to higher energy levels. This phenomenon is called absorption or transmission (equation 1.9):

$$A = -\log T = -\log \frac{\Phi}{\Phi_0} \qquad (1.9)$$

Where A is an absorbance, T is a transmittance, Φ is radiant flux transmitted by material, Φ_0 is radiant flux received by material.

Absorbance can be used as a tool for determination of concentration by Lambert – Beer law (equation 1.10):

$$A = \varepsilon L c \qquad (1.10)$$

Where ε is absorption coefficient, L is path length of the beam of light and c is concentration.

UV/VIS spectrometers contain source of light, monochromator and detector. As a source of the visible light, tungsten filament or halogen lamp are used and for the ultra violet a deuterium arc lamp is typically used. A Xenon arc lamp, on the other side, can provide both types of radiation. Moreover, this lamp does not need a time to warm up, but it is more expensive. Monochromator is an optical device that separate particular part of radiation at the input and only select part of wavelengths that are released at the output. The monochromator is usually representing by a grid or prism. Detector collects light that remain after sample irradiation. The CCD, photomultiplier or photodiodes serve as a detectors of UV/VIS light[93].

4.4 Raman spectroscopy

Another type of interactions of light with matter can be a light scattering that can be divided into elastic (Rayleigh) and inelastic (Raman) scattering. During Rayleigh scattering, electrons are excited by incoming photons to the higher energy level and then return to the basic energy level. Thus, this type of scattering is not carrying any analytical information. On the other hand, Raman scattering, discovered by Chandrasekhara Venkata Raman in 1928[94], provides analytical information due to Raman shift. Consequently, excited electrons can return to the higher or lower energy level than the energy level from which they were excited. In both cases, photons are emitted, and their wavelength may be greater when electrons return to higher energy level (Stokes photons) or their wavelength may be lower (Anti-Stokes photons) when electrons return to lower energy level compared to original energy level (Figure 9).

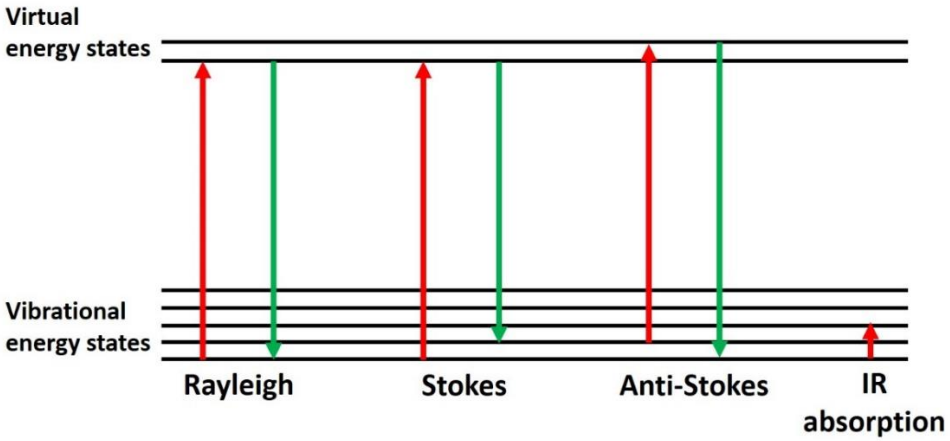

Figure 9 - Scheme of Rayleigh and Raman scattering (Stokes and Anti-Stokes photons)

An earlier radiation source in Raman spectroscopy was a mercury lamp. At present, the most used radiation sources are gas lasers (helium-neon or neodymium-YAG) that provide monochromatic visible or near infrared (IR) radiation. These low energy sources inhibit unfavourable fluorescence. Scattered radiation is observed in 90° or 180° direction to the direction of the incident radiation. Then, it is necessary to use monochromator that eliminates Rayleigh scattering. Finally, as detectors are used CCD or photomultipliers. Modern Raman spectrometers use interferometers and process data by Fourier transformation (FT). The biggest advantage of FT spectrometers are high measurement speed and higher signal intensity[93,95].

5 Aims of the diploma thesis

1) The preparation, characterization and photoelectrochemical examination of wide band gap semiconductors based on metal oxides represented by TiO_2 and WO_3 to be applied as photoanodes in PEC water splitting cells. The main focus is to deposit these materials in the form of nanorods onto the FTO substrate.

2) The preparation, characterization and photoelectrochemical examination of another photoanode material based on a narrow band gap material such as $BiVO_4$. The $BiVO_4$ is prepared by two different methods including chemical synthesis and electrodeposition.

3) Doping of $BiVO_4$ by foreign atoms such as Mo and W in order to improve the photogenerated charges dynamics and thus the PEC performance.

EXPERIMENTAL PART

Used chemicals:

Bismuth nitrate pentahydrate	Sigma Aldrich, 98%
Vanadyl acetylacetonate	Sigma Aldrich, 98%
Potassium iodine	Lachema N.P. Brno, 99%
p-benzoquinone	Sigma Aldrich, 98%
Sodium sulfate	Sigma Aldrich, 99%
Acetone	Honeywell, p.a.
2-propanol	Sigma Aldrich, p.a.
Dimethyl sulfoxide (anhydrous)	Sigma Aldrich, 99.9%
Ethylene glycol (anhydrous)	Sigma Aldrich, 99.8%
Nitric acid 65%	Penta, p.a.
Sodium hydroxide	Lach-Ner, p.a.
Bis(acetylacetonato) dioxomolybdenum(VI)	Sigma Aldrich
Sodium sulfite	Sigma Aldrich, p.a.
Triton X-100	Sigma Aldrich, laboratory grade
Ethanol absolute	BC-chemservis, p.a.
Sodium tungstate dihydrate	Sigma Aldrich, 99%
Sodium phosphate dibasic	Sigma Aldrich, 99%
Sodium phosphate monobasic	Sigma Aldrich, 99%
Ammonium (para)tungstate hydrate	Sigma Aldrich, 99.99 %
Chloric acid 35%	Penta, p.a.
Hydrogen peroxide 30%	Sigma Aldrich,
Titanium (IV) butoxide	Sigma Aldrich, 97%

6 Preparation of thin films

In this diploma thesis, few different types of photoactive films were prepared on to the most commonly used transparent conductive substrates for photoelectrochemical application such as a glass substrate coated by a conductive fluorine doped tin oxide ($F:SnO_2$, FTO) conductive layer. These substrates went always through the same cleaning procedure that included 30 minutes of sonication in mixture of acetone, 2-propanol and water (1:1:1). Firstly, WO_3 nanorods were grown in an autoclave by a hydrothermal method. The as prepared amorphous WO_3 nanostructures were subsequently annealed in air at different temperatures to provide their crystallization. Analogously, TiO_2 thin films with similar nanorods structure were prepared also in autoclave under the hydrothermal conditions with subsequent annealing procedure. Finally, the $BiVO_4$ photoanodes were prepared by a drop casting method exploiting Triton X-100 surfactant as a structure agent. Second approach for $BiVO_4$ preparation was based on a twostep procedure: using first an electrodeposition of BiOI nanosheets, which were in the following step converted by vanadium solution and subsequent annealed into the desired $BiVO_4$ nanostructured films. Among the all studied materials particular attention was devoted to $BiVO_4$.

6.1 Preparation of TiO_2

In typical synthesis, TiO_2 thin films were prepared by adding 0.46 ml of titanium butoxide to the solution containing 14 ml of water and 14 of concentrated HCl. This solution was stirred for half an hour. Therefore, autoclave was filled by as prepared solution and FTO was putted into that solution by conductive side facing down. The reaction in the autoclave was run for 10 hours at 150 °C in a furnace. The as prepared TiO_2 layers were annealed at 450 °C for 1 hour to obtain a crystalline structure.

6.2 Preparation of WO_3

The WO_3 nanorods were fabricated by dissolving 1g of ammonium (para)tungstate in 95 ml water with 3 ml of concentrated HCl. Then, solution was stirred until yellow gelatine precipitate appear. After that, 2 ml of H_2O_2 was added and as prepared mixture was stirred for 1 hour. Solution was transferred into autoclave and FTO substrate was submerged into the solution with the conductive side facing down. Autoclave was exposed to 160 °C for

4 hours. Then, FTO with the grown WO_3 layer was taken out of the autoclave and annealed at 500 °C for 1 hour.

6.3 Preparation of $BiVO_4$ by drop casting

The preparation of $BiVO_4$ by the drop casting method included Triton X-100 as a structure agent. Bismuth solution was prepared by dissolving 0.22 g $Bi(NO_3)_3$ in 6ml of ethylene glycol (75 mM) and likewise vanadium solution was prepared by dissolving 0.12 of $VO(acac)_2$ in 6 ml of ethylene glycol (75 mM). Then, 1%, 5% or 10% of Triton X-100 was added into 1 ml of ethylene glycol. Therefore, bismuth, vanadium and triton solutions were mixed together in the ratio of 2:2:1. Next the 100 μL of the mixed solution was drop casted on the FTO which was partially covered by teflon tape due to ensuring an electrical contact for the following electrochemical measurements. Finally, the samples were dried for 1.5 hours at 60 °C and were annealed for 2.5 hours at 500 °C.

6.4 Electrodeposition of BiOI

BiOI was used as a precursor for $BiVO_4$. The electroplating solution was prepared by dissolving 40 mM $Bi(NO_3)_3$ in a 50 ml of 400 mM KI water solution. This solution was adjusted by HNO_3 to pH 1.7. Then, 230 mM of p-benzoquinone was added to 20 ml of absolute ethanol and then mixed together with previous solution. Three electrodes were submerged into this mixed solution – reference electrode (Ag/AgCl with 3M KCl solution) (RE), counter (CE) and working (WE) electrodes which were represented by FTO substrates. The photograph of the experimental set-up is shown in Figure 10. The substrates were initially cleaned at mixture of acetone, 2-propanol and water 1:1:1 and ultrasonicated for 30 minutes.

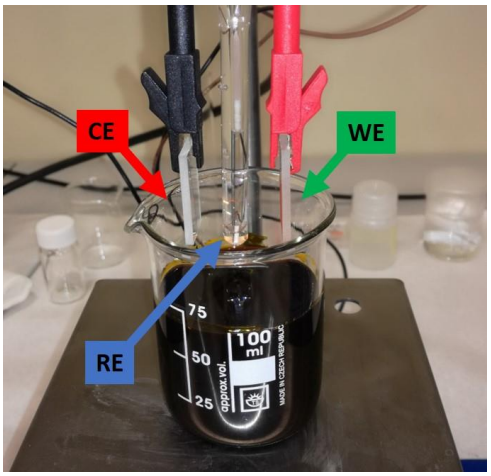

Figure 10 - Electrodeposition of BiOI and description of electrodes in solution

Electrodeposition was proceeded at -0.2V at various times (30, 60, 120, 240 s). The Applied potential causes reduction of p-benzoquinone to hydroquinone at the WE. This process is associated with consuming H^+ ions, which consequently leads to a local increase of pH and thus to precipitation of crystalline BiOI on the WE[96]. The as-deposited BiOI films on the FTO substrates were dried under ambient conditions.

6.5 Conversion of BiOI to $BiVO_4$

Electrochemically deposited BiOI films were in the synthetic step transformed into the $BiVO_4$ by following procedure. The dried BiOI samples were homogeneously covered by a solution mixture of 150 μL of 200 mM vanadyl acetylacetonate in anhydrous dimethyl sulfoxide (DMSO). Such treated samples were then placed into a furnace and annealed for 2 hours at 450 °C with the temperature rate of 2.5 °C per minute. The exact temperature ramp is schematically shown in Figure 11.

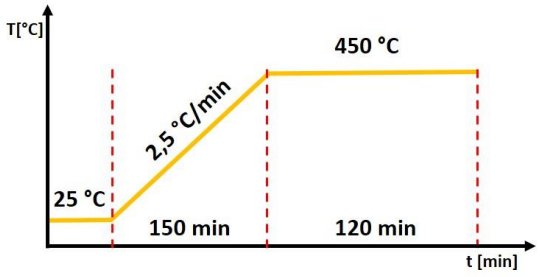

Figure 11 - Scheme of annealing procedure

The annealing procedure causes decomposition of BiOI into Bi_2O_3 and I_2 that sublimes. The Bi_2O_3 subsequently reacted with vanadyl acetylacetonate to form $BiVO_4$[96]. After the annealing, the samples were washed in 1 M NaOH for 30 minutes while stirring due to removing of V_2O_5 excess (Figure 12).

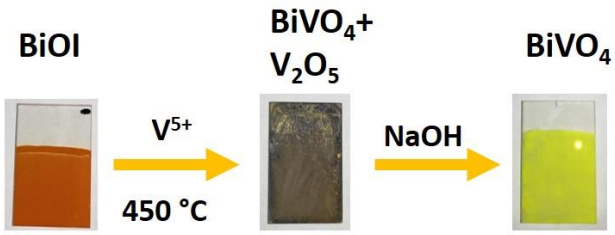

Figure 12 - Scheme of BiOI conversion in to $BiVO_4$

6.6 Doping of $BiVO_4$ by Mo and W

After BiOI conversion in to $BiVO_4$, samples were doped by molybdenum and tungsten. For this purpose, a molybdenum solution was prepared by dissolving 5mM bis(acetylacetonato) dioxomolybdenum in DMSO and similarly tungsten solution was prepared by dissolving 5 mM sodium tungstate in DMSO. Then, 12 µL of molybdenum solution was drop casted on the $BiVO_4$ surface and 12 µL of tungsten solution was drop casted on another $BiVO_4$ sample. Samples were annealed for 2 hours at 450 °C with temperature rate 2.5 °C/minute. After the annealing procedure, samples were also washed in 1 M NaOH for 30 minutes while stirring.

7 Diagnostic of layers

7.1 Physical characterization

Several characterization techniques were used to determine the basic physical properties of the prepared samples. These measurements included:

- X-Ray diffraction measurements were proceeded by Empyrean device (PANalytical, Netherlands) with Co lamp producing K alpha radiation, focusing mirror, programmable secondary anti-scattering clone and fast position sensitive Pixcell detector.

- SEM images were taken by Hitachi SU6600 in secondary electron regime with Schottky cathode as a source of electrons. For top view images, accelerating voltage was set to 5kV and 3kV for cross section images.
- UV/Vis spectra were collected on FLS980 fluorescence spectrometer (Edinburg instruments Ltd, Great Britain) with photomultiplier and with 450 W Xe arc lamp as a source of light.
- Raman spectra was taken by Raman DXR (Nicolet, USA). Laser has intensity 5mW with exposition time 5 s.
- XPS spectra were captured by PHI 5000 VersaProbe II (Physical Electronics, USA) with monochromatic Al K_α as a source of X-ray radiation

7.2 Photoelectrochemical characterization

Photo – induced electrochemical analysis was performed using three electrode system. All photoelectrochemical measurement were proceeded by Gamry Instruments potentiostat Series G 300. As a reference electrode a Ag/AgCl electrode in environment of 3 M KCl was used and platinum wire introduced a counter electrode. A solar simulator LOT LS0106 with 150 W Xenon lamp (Figure 13) equipped by an AM 1.5 filter was employed for light induced measurements. The prepared and tested samples were always employed as a photoanode and were illuminated from the front side using the light with intensity of 100 mW/cm^2. The whole photoelectrochemical set-up is shown at Figure 14.

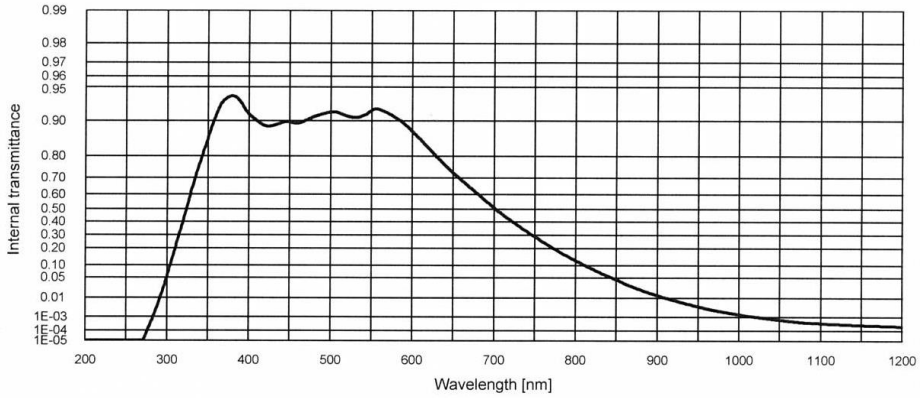

Figure 13 - Transmittance spectrum of Xe lamp

Photoelectrochemical measurements include many basic characteristics such as photocurrent density, open circuit potential, voltage or impedance spectroscopy. Bellow, these techniques are described.

- Sweep linear voltammetry (LSV) – This method studies changing current (or photocurrent in dark or under illumination) at working electrode while potential between reference and working electrode is linearly increasing. Measured photocurrent was recalculated to the area of the sample of 1 cm^2 (photocurrent density) and the scan rate of the applied voltage to the WE was set to 10 mV/s.
- Chronoamperometry (ChAM) – This technique monitors photocurrent density over a time period while the applied potential on the WE is constant. Potential was mostly set at 0.5 V vs. Ag/AgCl, but in few cases it was necessary to use different potential. Sample was illuminated at the 30s/60s intervals of dark/light period.
- Electrochemical impedance spectroscopy (EIS) – Alternating current with sinusoidal waveform flowing through the cell behaves as an impedance probe with real and imaginary parts due to the ohmic resistance and capacitance of the electrolyte. These capacitance and resistance can be replaced by substitute circuit with parts such as condensers or resistors. Thus, this method measures impedance as a function of frequency and then the achieved data can be converted into Nyquist diagram. Each point of Nyquist diagram corresponds to impedance at one frequency and measurement is proceed at constant voltage[97]. Applied frequency was in range 0.1 – 10^5 and applied voltages were 0.3 V and 0.5 V.

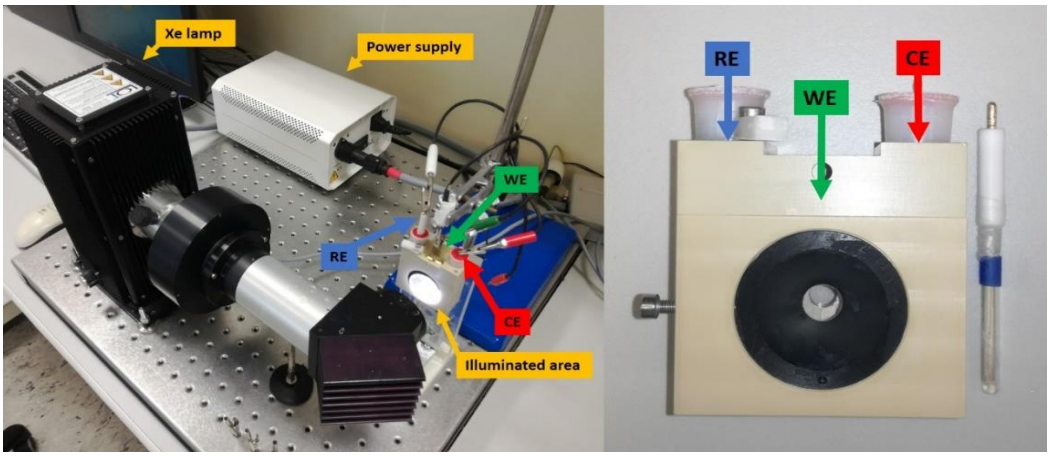

Figure 14 - Photoelectrochemical setup

8 Results and discussion

This chapter will show physical characterization and photoelectrochemical measurements results of WO_3 and TiO_2 prepared hydrothermally. $BiVO_4$ prepared by drop casting and by conversion from BiOI prepared by electrodeposition will be the main topics of this chapter. Also, BiOI results will be discussed as a photoactive intermediate layer (precursor layer) for the $BiVO_4$ conversion.

8.1 Titanium dioxide (TiO_2)

Titanium dioxide in the form of nanorod arrays was prepared by the hydrothermal method and then subsequently annealed in air at 450 °C for 1 hour. Firstly, the resulted white films were studied by SEM. Figure 15 A and B reveal surface that is homogenously covered by oriented nanorods which was similarly observed also in other works, e.g. in the reference 98[98]. Figure 15 C shows XRD patterns that confirms rutile structure of hydrothermally prepared nanorods as it corresponds to 01-072-7374 PDF+- from ICDD database. The electrochemical properties were measure by linear sweep voltammetry (LSV) in 1M NaOH electrolyte. TiO_2 performs around 0.5 mA/cm^2 at 0.5 V versus Ag/AgCl electrode. This relatively small photocurrent is caused by poor UV/VIS absorption of TiO_2.

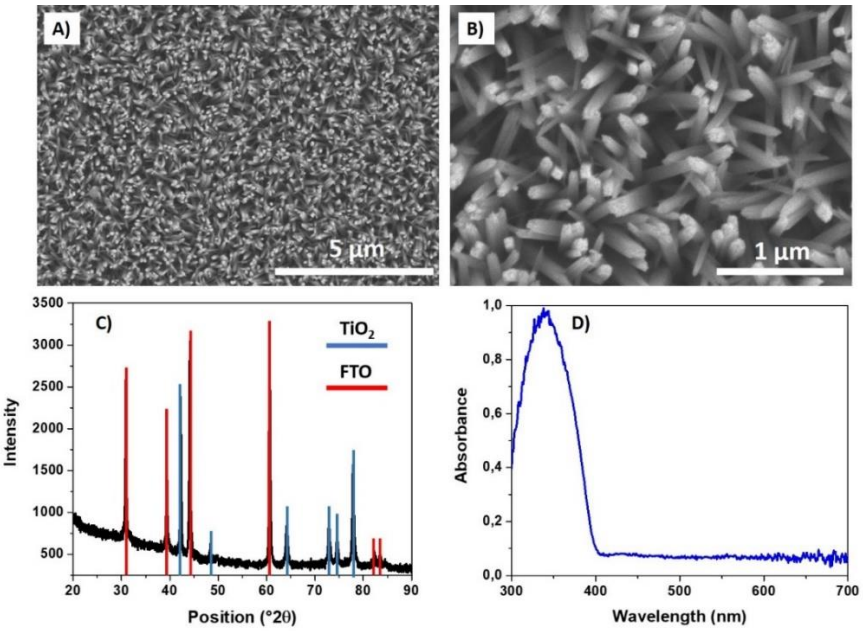

Figure 15 - TiO_2 thin films A), B) SEM images, C) XRD pattern and D) Absorbance spectra

Absorption of TiO_2 (Figure 16) is the biggest disadvantage of this photoactive material because this rutile TiO_2 have absorbance maximum at around 350 nm and then rapidly declines. Sunlight contains only 6% of UV radiation[43] and so this material is not suitable for practical application for the direct solar water splitting. This key drawback can be addressed by different strategies such as elemental doping (e.g. N) to narrow the band gap width or by using external optical sensitizers such as various organic dyes, quantum dots, plasmonic particles, etc. However, these approaches were not the subject of this thesis.

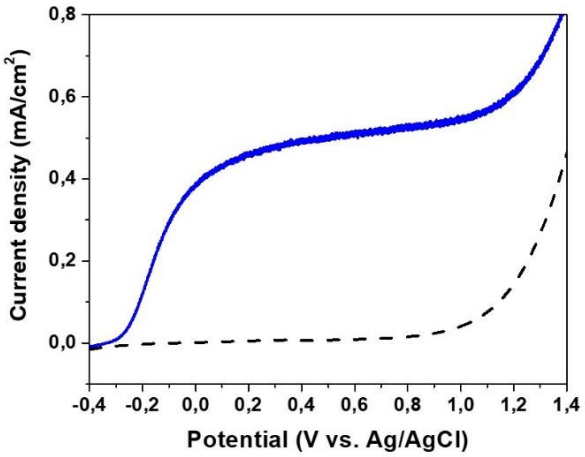

Figure 16 – LSV measurement in 1M NaOH. Black dotted line represents dark part of measurement

8.2 Tungsten trioxide (WO_3)

Tungsten trioxide is another n-type metal oxide semiconductor used as the photoanode material for the PEC water splitting. WO_3 was prepared similarly as the TiO_2 nanorods by the two step procedure including hydrothermal synthesis and following annealing treatment. Figure 17 A and B show the surface SEM morphology WO_3 images denoting a homogenous coverage of the FTO substrate by randomly oriented nanorods with various length. The XRD pattern (Figure 17 C) match with the reference XRD card 04-005-4272 from PDF-4+ 2016 ICDD database that confirm monoclinic crystalline phase. The photoelectrochemical properties of WO_3 nanorods were investigated by means of LSV experiments. The measurements were proceeded in PBS + 0.1M Na_2SO_3 working as the electrolyte and the results are shown in Figure 18.

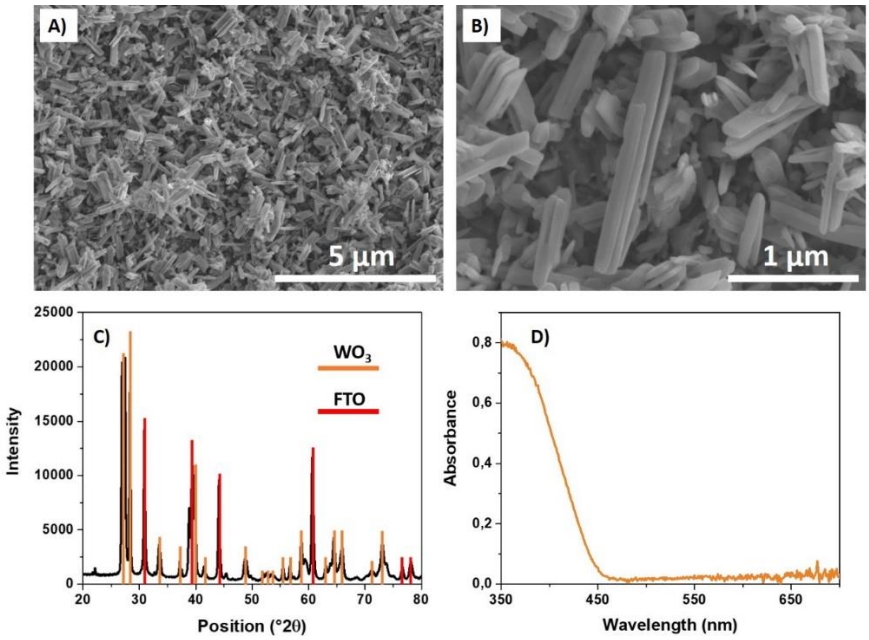

Figure 17 - WO_3 prepared by hydrothermal method. A) and B) SEM images, C) XRD pattern D) absorbance spectra

WO_3 suffers also from poor absorbance in VIS region as it can be seen in Figure 17 D. It has absorbance maximum near to 350 nm but then it decreases to the 450 nm where there is no any absorption (Figure 18). Absorption in UV region is related to the poor photoelectrochemical performance despite homogenous nanorods surface and high crystallinity. Due to this handicap WO_3 is commonly used in a conjunction with other semiconductor such as a $BiVO_4$ representing photoanode with wider absorbance range and thus narrower band gap compared to WO_3 or TiO_2.

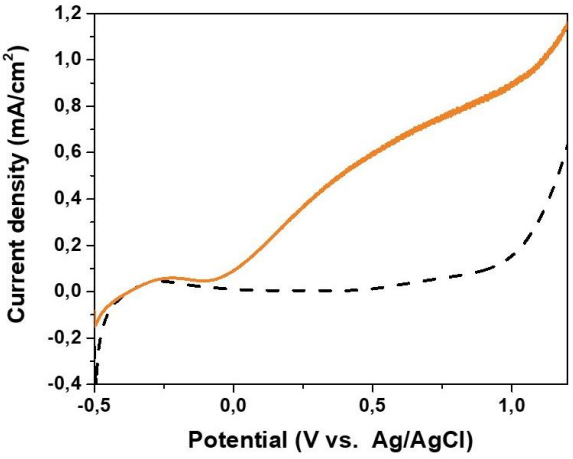

Figure 18 – LSV measurement in PBS + 0.1M Na_2SO_3. Black dotted line represents dark part of measurement

8.3 Bismuth vanadate ($BiVO_4$)

Among all three semiconductors investigated in this diploma thesis the particular attention was given to bismuth vanadate. It has been identified as one of the most promising photoanode materials for PEC water splitting owing to its suitable band gap energy and the other aforementioned beneficial features. Despite apparent topicality this material is still rather understudied and thus for the rest of this thesis I focused exclusively on the experimental investigation of $BiVO_4$.

Bismuth vanadate was prepared by two different methods. Firstly, the $BiVO_4$ precursors were drop casted on the surface of the FTO substrate. The solution with three various concentrations of Triton X100 in ethylene glycol was used as a structure agent. However, prepared layers were not sufficiently homogenous and produce low values of photocurrent. Electrodeposition of BiOI and subsequent conversion in to BiVO4 offers more controllable method of preparation homogenous layers with considerably higher photoactivity.

8.3.1 Preparation of $BiVO_4$ by drop casting

Triton X-100 surfactant was added to three ethylene glycol solutions in different concentrations (1%, 5% and 10%) and then the Triton X-100 containing solution was mixed with bismuth and vanadium ethylene glycol solutions. After drying at 60 °C for 1.5 hours and annealing at 500 °C for 2.5 hours the samples were characterized and measured.

Firstly, the samples were analysed by SEM. Following images (Figure 19) revealed aggregation of $BiVO_4$ particles. Figure 19 A.1 and A.2 reffer to sample prepared with 1% of Triton X-100 and this concentration causes starting aggregation while Figure 19 B.1 and B.2 correspond to the sample prepared with 10% of Triton X-100 and it shows that the film completely aggregated.

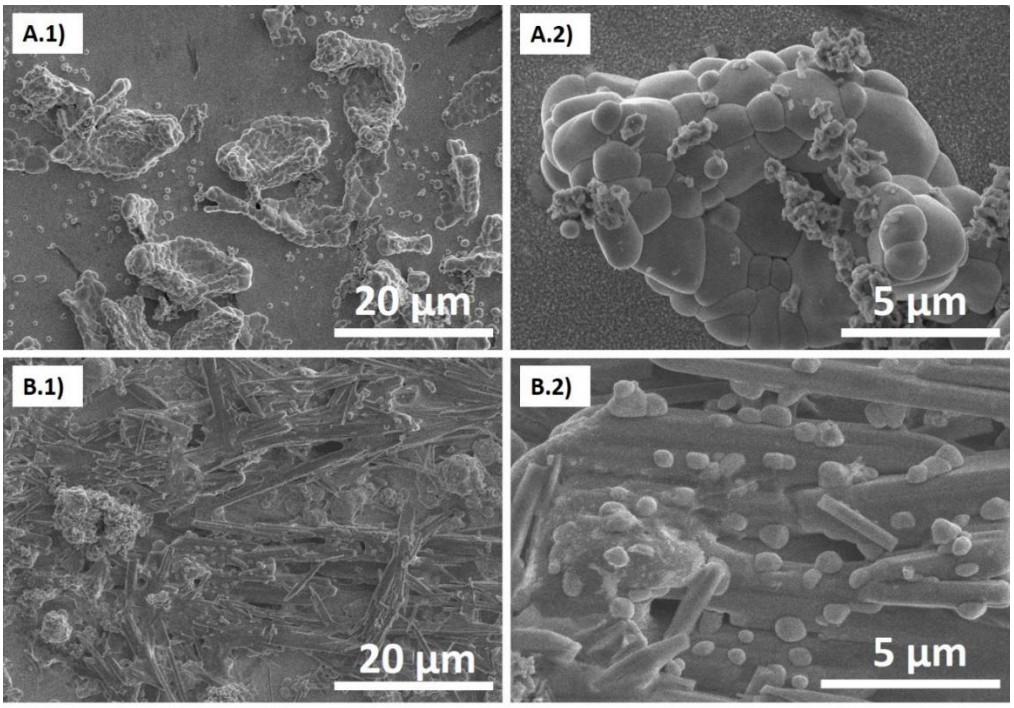

Figure 19 - $BiVO_4$ prepared by drop casting method. A.1) and A.2) 1% of Triton X-100. B.1) and B.2) 10% of Triton X-100

EDS spectrum shows peaks of bismuth, vanadium and oxygen which leads to $BiVO_4$. Other peaks such as particularly tin are caused by FTO substrate. XRD analysis investigated crystalline structure of $BiVO_4$ prepared by drop casting method.

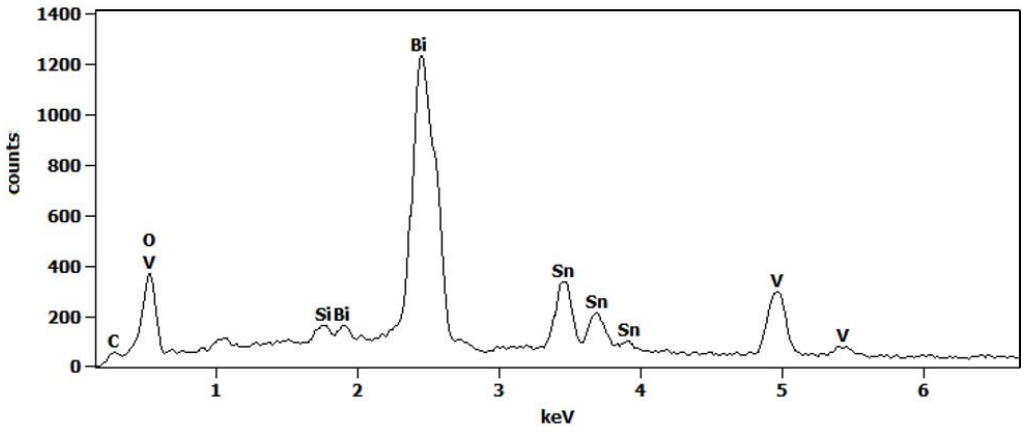

Figure 20 - EDS spectrum of $BiVO_4$ prepared by drop casting method with 10% of Triton X-100

Figure 21 shows XRD peaks marked by a green colour are indexed to clinobisvanite – monoclinic form of $BiVO_4$ (04-010-5713, PDF-4+ 2016 ICDD database). Purple lines

represent different crystalline phases of $BiVO_4$. Therefore, we can conclude that the presented chemical synthesis and drop casting deposition yielded $BiVO_4$ films with different crystalline structures. Red lines belong to FTO substrate (04-016-0597, PDF-4+ 2016 ICDD database).

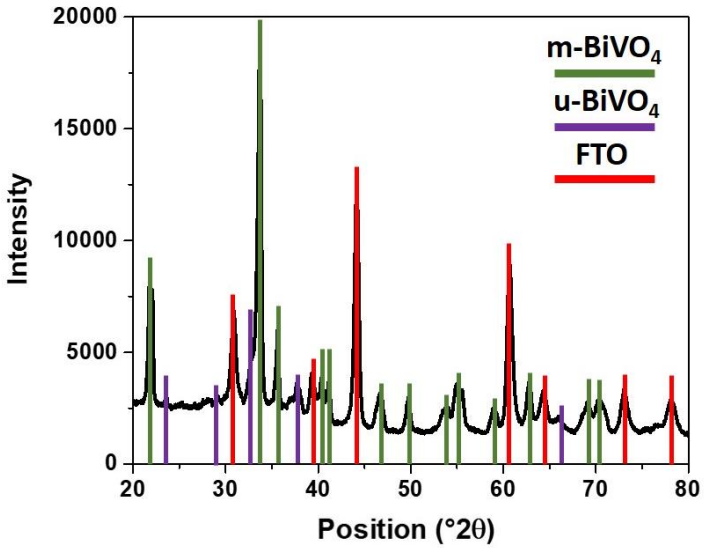

Figure 21 – XRD patterns of $BiVO_4$ prepared by drop casting method with 5% of Triton X-100. Green lines represent monoclinic phase of $BiVO_4$ and purple lines represent unidentified $BiVO_4$ phases

Next characterization technique is Raman spectroscopy which is able to probe local structure of materials because the bonding states in the polyhedral can be deducted directly from spectrum. Layers prepared with solution containing 1% and 10% of surfactant were chosen for this analysis.

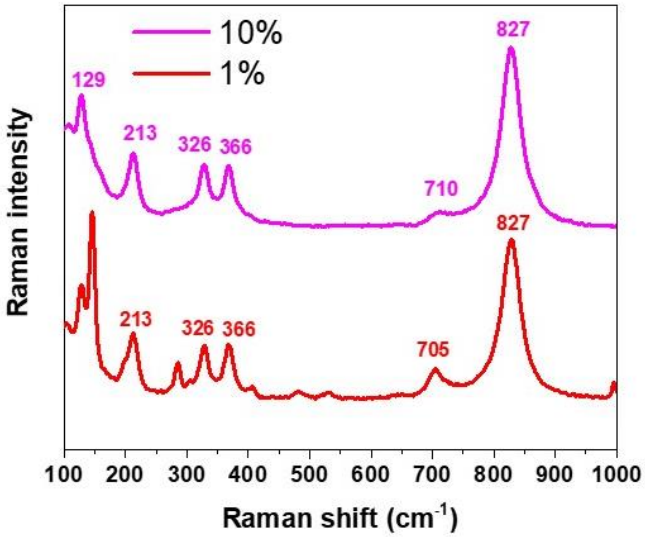

Figure 22 – Raman spectra of $BiVO_4$ prepared with 1% and 10% of Triton X100 as a structure agent

Raman spectra of $BiVO_4$ (Figure 22) are characteristic by main peak at 827 cm^{-1}, which together with peak at 710 cm^{-1} is caused by V – O symmetric stretching. Peaks 326 cm^{-1} and 366 cm^{-1} can by assigned to the symmetric and asymmetric deformation mods of VO_4 tetrahedrons. Peaks 129 cm^{-1} and 213 cm^{-1} are related to the external mode of $BiVO_4$[99,100]. This spectrum can give us also information about phases of $BiVO_4$ because biggest peak located at 827 cm^{-1} corresponds to clinobisvanite, which is monoclinic form of $BiVO_4$[101]. Spectrum of 1% Triton X100 solution contains, besides typical $BiVO_4$ peaks, few unknown peaks. On the other hand, spectrum of 10% solution shows only typical $BiVO_4$ peaks.

Electrochemical properties of $BiVO_4$ prepared by drop casting method were investigated by linear sweep voltammetry (LSV) as it is shown in Figure 23. All measurements were carried out in the environment of 0.1M Na_2SO_4. At lower potential, 5% and 10% performed better photocurrent but at higher potentials the samples prepared with 1% and 5% become similar and 10% declines.

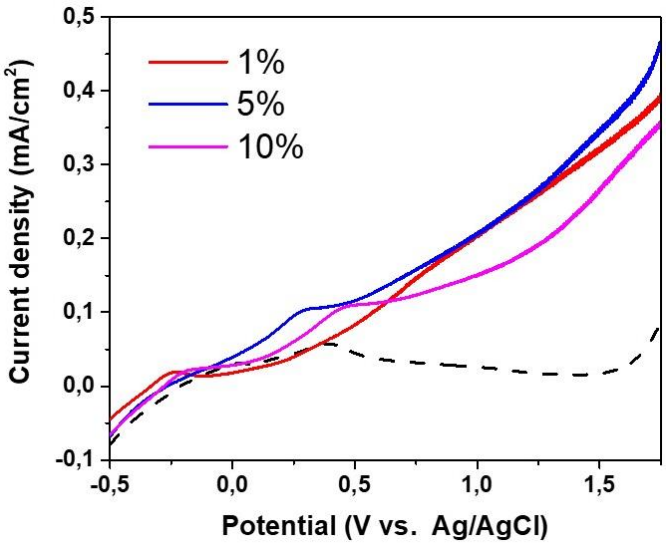

Figure 23 – LSV measurement of three concentrations of structure agent Triton X100. Measured in 0.1M Na_2SO_4. Black dotted line represents dark part of measurements

As prepared samples performed poor photocurrent density and according to the characterization techniques, structure of observed $BiVO_4$ were not pure monoclinic but there were also others unknown phases. In this case the different crystalline structures worked as an impurity and the high probability causing a high extent of backword recombination of the photogenerated charge carriers such as electron and hole pairs. Besides these handicaps, drop casted films were not so mechanically stable and it was easy to brush them away. For these reasons, it was necessary to find different and more convenient method for the $BiVO_4$ preparation.

8.3.2 Electrodeposition of BiOI

This method was chosen due to good homogeneity of final layers compared to drop casted layers. Following SEM images displayed in Figure 24 show surface of BiOI prepared by 120 s of electrodeposition. Figure 24 A confirms the high homogeneity of surface coverage by the grown BiOI film. On the other side, this SEM image also reveals several sphere-like artefacts randomly distributed over the film, which was a common feature of the grown films by the electrodeposition. Figure 24 B shows detail of BiOI structure that is composed of sheets-like units with edge length around 1 μm in average and thickness of tens of nanometers.

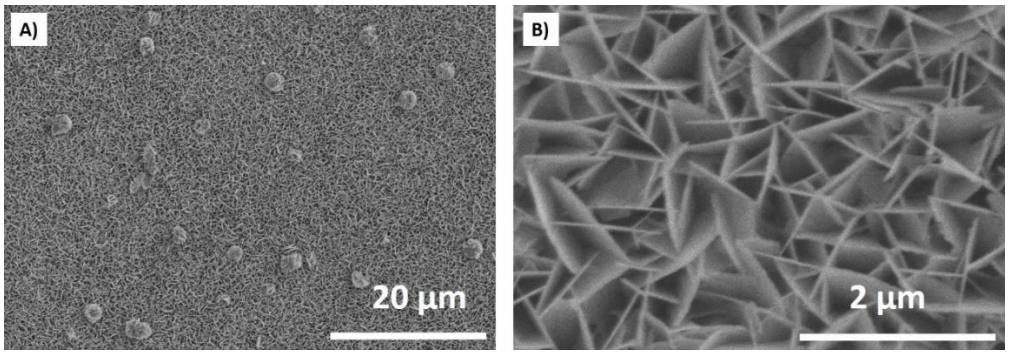

Figure 24 – SEM images of BiOI prepared by 120 s of electrodeposition

In the following experiments I carried out the electrodeposition with four various times such as 30, 60, 120, 240 s. In Figure 25 the cross section images of such prepared films are seen revealing the structure changes with the electrodeposition time increase. In the beginning of the electrodeposition, the material starts stick to the surface of FTO substrate (Figure 25 A). After 60 s, sheets-like structure appears with 750 nm average height (Figure 25 B). With increasing time, sheets grow to around 1 µm (Figure 25 C). When electrodeposition time reaches 240s, sheets start to collapse and peeled off the FTO substrate (Figure 25 D).

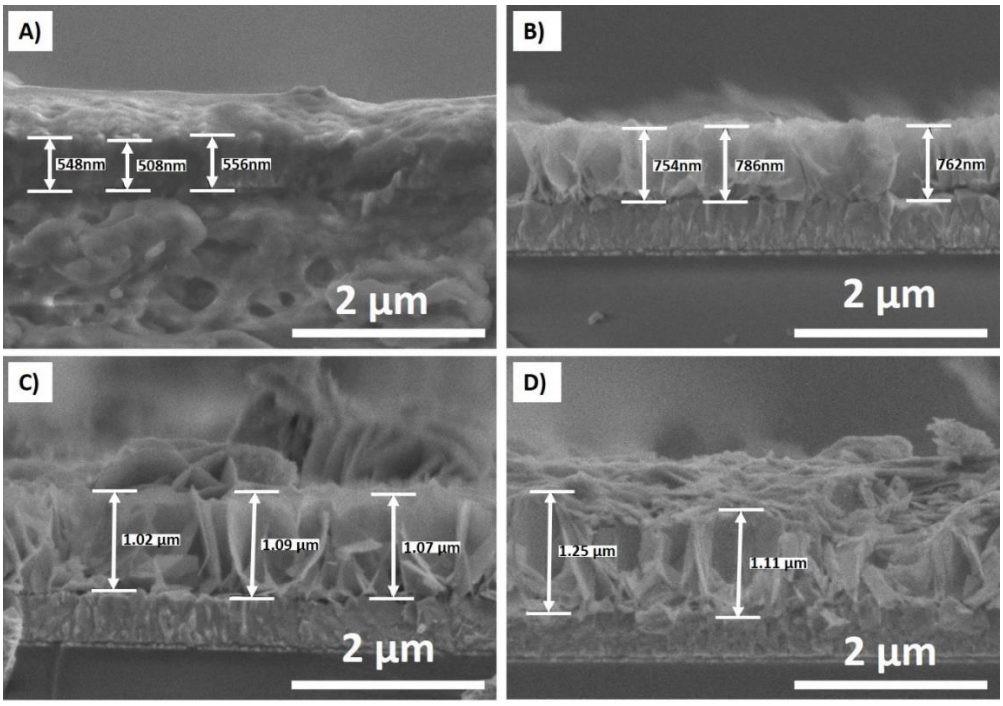

Figure 25 - SEM cross section images of BiOI prepared by four electrodeposition times. A) 30 s B) 60 s C) 120 s D) 240 s

During SEM measurements of the sample electrodeposited for 120 s also EDS spectrum was recorded (Figure 26) that confirms presence of bismuth, iodine and oxygen lacking any contaminants. The tin peaks belong to the FTO substrate. The very high intensity of these Sn peaks are due to highly porous nanosheet-like morphology and thus the electron beam can easily reach the FTO substrate.

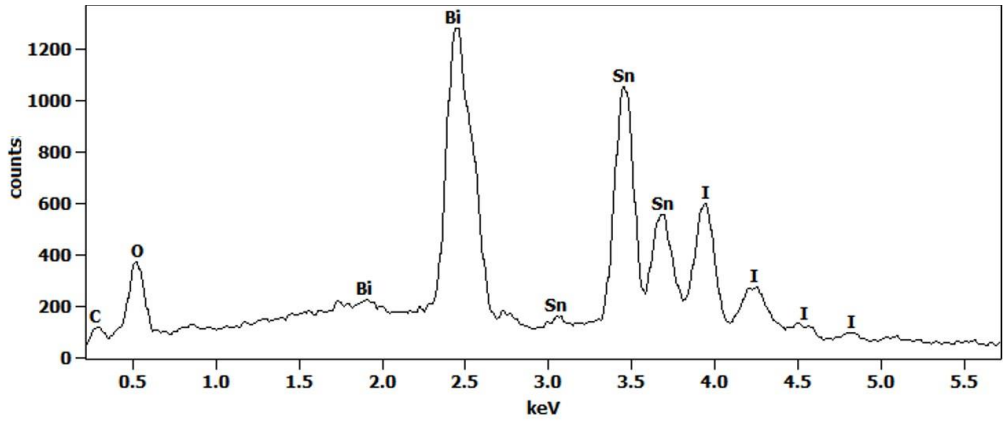

Figure 26 - EDS spectrum of BiOI prepared by 120 s of electrodeposition

The XRD patterns (Figure 27) of samples prepared by 120 s of electrodeposition agreed with tetragonal BiOI structure. Thus, crystal structure was confirmed (00-010-0445; PDF-4+ 2016 ICDD database). Other residual peaks were observed due to FTO substrate. EDS spectra and X-ray diffractogram definitely confirmed the presence of crystalline BiOI.

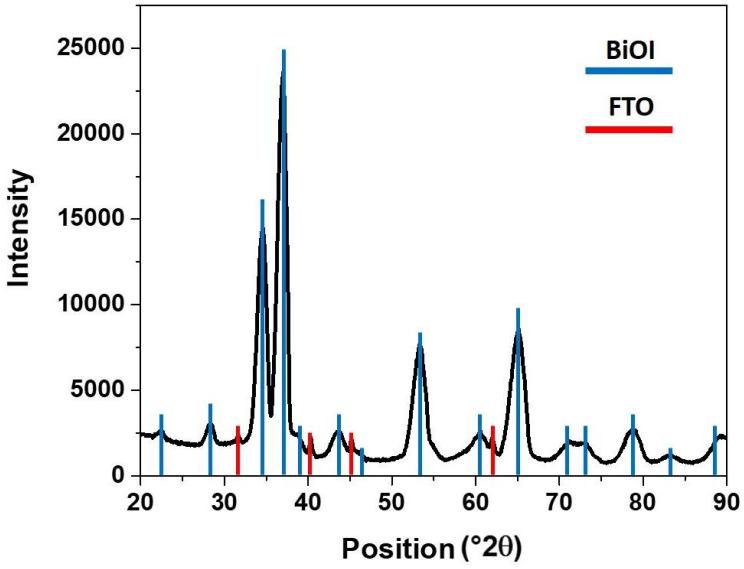

Figure 27 - XRD patterns of BiOI prepared by 120s of electrodeposition

The absorbance spectra (Figure 28) show that as prepared BiOI absorbs in broad range of UV/VIS radiation from 350 nm to 525 nm where absorbance starts decreasing. Moreover, it is clearly observed that electrodeposition time play also a significant role. With increasing electrodeposition time, BiOI absorb more visible light. Absorbance of BiOI prepared by 30 s of electrodeposition begin to decrease at almost 475 nm while BiOI prepared by 240 s of electrodeposition absorb till almost 550 nm.

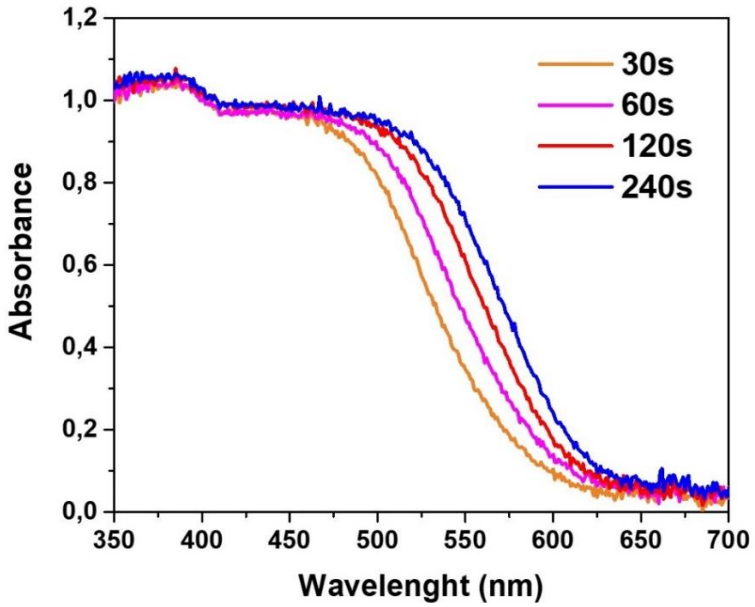

Figure 28 - UV/VIS spectra of BiOI prepared by various electrodeposition time

These spectra agree with LSV measurements (Figure 29) where the samples were exposed to linearly increasing potential in 0.1M phosphate buffer solution (PBS) with pH 7. Among other samples, BiOI electrodeposited for 240 s performs best photocurrent density, which is due to the extended light absorption. In contrast, the 30 s of electrodeposition was not enough to observe any significant photocurrent. Despite all these results, as prepared BiOI is not suitable material for the direct water splitting and served only as a precursor for $BiVO_4$ conversion due to its chemical stability.

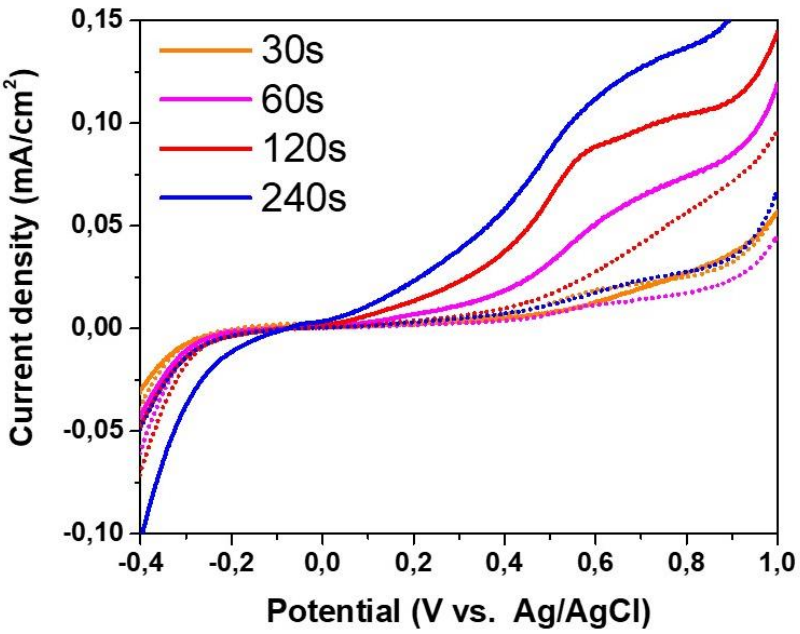

Figure 29 - BiOI prepared by different electrodeposition time. Solid lines represent light part of measurements and dotted lines represents the dark part of measurements. All samples were measured in PBS.

8.3.3 BiOI conversion in to $BiVO_4$

BiOI prepared at different electrodepositing times were converted in to $BiVO_4$ by adding DMSO solution of vanadyl acetylacetonate on the surface of the BiOI precursor layer and the subsequent annealing at 450 °C for 2 hours with temperature rate 2.5 °C /min. These layers were much more homogenous compared to drop casting method as well as much more mechanically stable. The samples prepared by 120 s of electrodeposition was set as a standard for characterization techniques due to its best photoelectrochemical performance which will be discussed below.

As prepared samples were characterized by SEM showing their surface morphology. During these measurements the EDS spectrum was also captured.

The SEM images (Figure 30) demonstrate nanoworm-like structure which is larger then the BiOI nanosheets-like structure. This change is evolved during annealing due to contracting of 2D structured sheets in to round particles. These structures were observed also at others works[102,103].

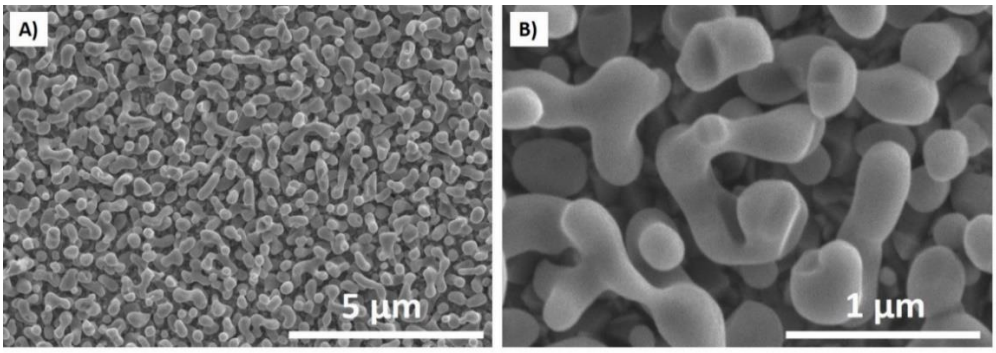

Figure 30 - SEM images of BiVO4 which was made by conversion from BiOI that was prepared by 120 s of electrodeposition

The EDS measurements (Figure 31) confirm presence of $BiVO_4$ thanks to bismuth, vanadium and oxygen peaks. Tin peaks appeared in the spectrum because of the FTO substrate.

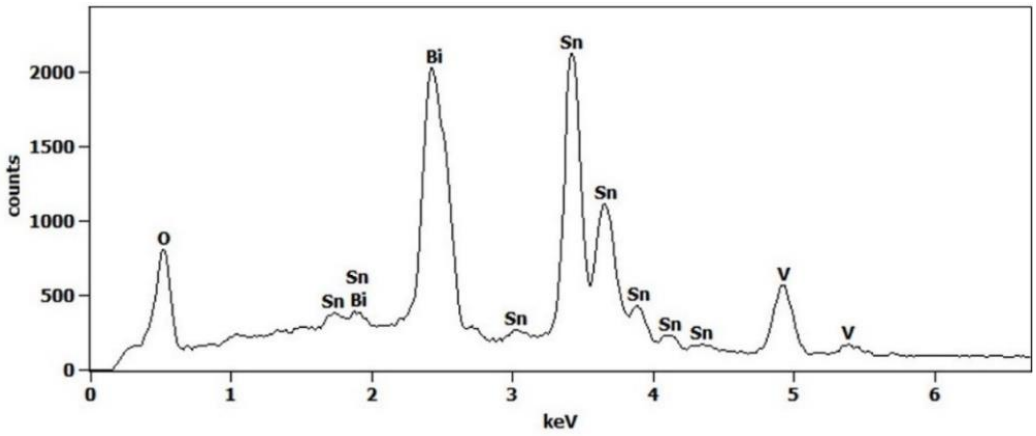

Figure 31 – EDS measurement of BiVO4 which was made by conversion from BiOI that was prepared by 120 s of electrodeposition

By comparing the BiOI structure in Figure 25 and resulting $BiVO_4$ in Figure 32 i.e. the dependency of electrodeposition time on the final morphology of $BiVO_4$ films it was revealed that the starting BiOI structure had a significant impact on the resulting morphology of $BiVO_4$ layers. Figure 32 A shows that small amount of starting (BiOI) material forms only few $BiVO_4$ particles on the sample surface after the thermal reaction. While the worm-like particles homogenously spread on the whole surface was clearly observed in Figure 32 B representing the electrodeposition time of 120 s. When $BiVO_4$ is converted from bigger BiOI sheets, the final $BiVO_4$ particles also grow bigger

(Figure 32 C). Interestingly, when BiOI is deposited for 240 s, the evolving worm-like sheets start to break down and during annealing with vanadium solution, as prepared $BiVO_4$ particles aggregate together and finally form bigger particles with sparse surface distribution (Figure 32 D).

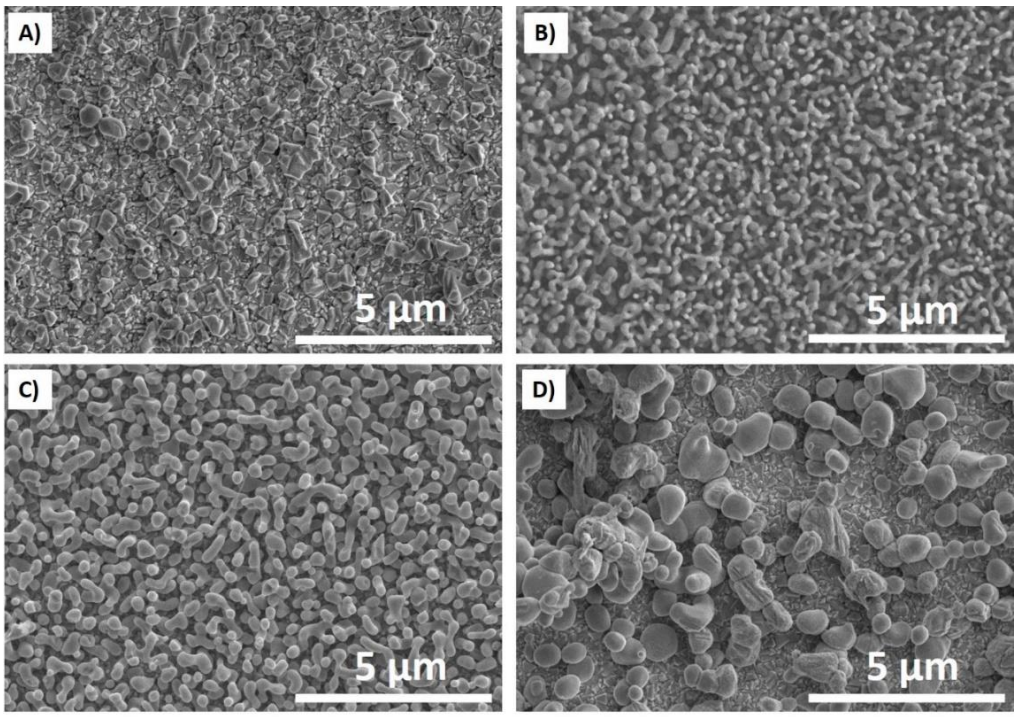

Figure 32 – SEM images of $BiVO_4$ prepared by converting from BiOI that was prepared by various electrodeposition times. A) 30 s B) 60 s C)120 s D) 240 s.

XRD analysis confirmed the presence of monoclinic $BiVO_4$ which is indicated by the green lines in Figure 33. The diffractograms of $BiVO_4$ show that films are highly crystalline and free from other crystal structures (04-010-5713, PDF-4+ 2016 ICDD database).

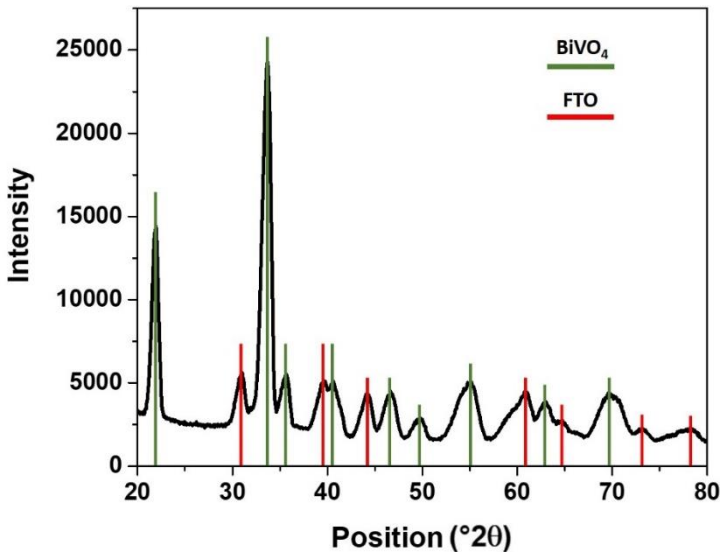

Figure 33-XRD patterns of BiVO4 which was made by conversion from BiOI that was deposited for 120 s

Raman spectra (Figure 34) further revealed the structure of $BiVO_4$ prepared by conversion from BiOI that was deposited for 120 s. It shows peaks significant for monoclinic form of $BiVO_4$ called clinobisvanite, as was mentioned before. Beside highest peak, spectra contained other $BiVO_4$ significant peaks such as 710, 366, 326, 213, 129 cm^{-1} [99,100].

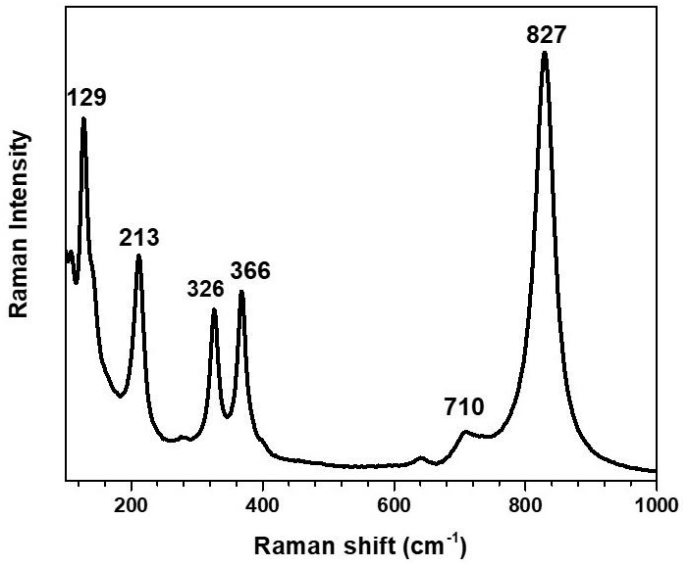

Figure 34 – Raman spectra of $BiVO_4$ which was made by conversion from BiOI that was deposited for120 s

The absorbance spectra shown in Figure 35 denote optical properties of the $BiVO_4$ samples. Compared to BiOI absorbance spectra (Figure 28), for the $BiVO_4$ films any significant shift of the absorption edge in the visible part was not observed. $BiVO_4$ layers start to absorb photons at UV region around 350 nm and absorption drops sharply around 470 nm. Another feature that can be read from the absorption spectra is that the time of electrodeposition affected the absorption in the order that it increased with the increased time of electrodeposition reaching the maximum for 120 s. On the other hand, this trend can be expected since the absorption increase observed is due to the increased thickness of the films. Further increase of the electrodeposition time, however, led to a collapsed and thus inhomogeneous structure, which resulted in the decreased absorption. This is perfectly in line with SEM morphology results which showed $BiVO_4$ prepared by conversion from BiOI electrodeposited for 120 s as a sample with largest surface and on the other hand, $BiVO_4$ converted from BiOI electrodeposited for 30 and 240 s as the samples with the smallest active surface.

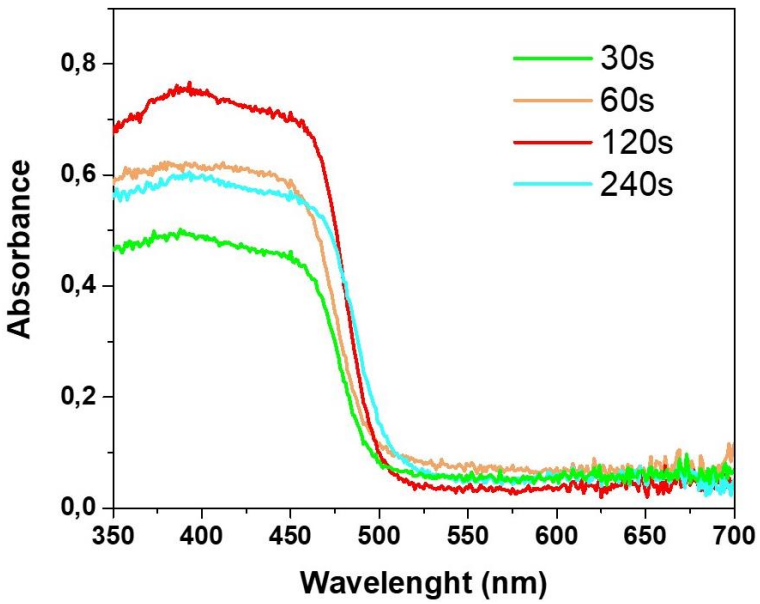

Figure 35 - UV/VIS spectra of $BiVO_4$ prepared by conversion from BiOI that was prepared by various electrodeposition time

Furthermore, the absorbance spectra matched with photoelectrochemical linear sweep voltammetry measurements (Figure 36) which also reflected the effect of BiOI electrodeposition on resulting $BiVO_4$ PEC performance. It is obvious that the 120 s sample had the highest homogeneity and relatively optimal thickness, which resulted in

the highest incident light absorption and finally also the highest photocurrent. The 60 s sample performed the second highest photocurrent density. These two samples with highest photoactivity had also the most homogenous surface with well distributed worm-like nanoparticles (Figure 32 B and C). On the other hand, samples with poor surface particles distribution reported the lowest photocurrent density as well as the low absorbance.

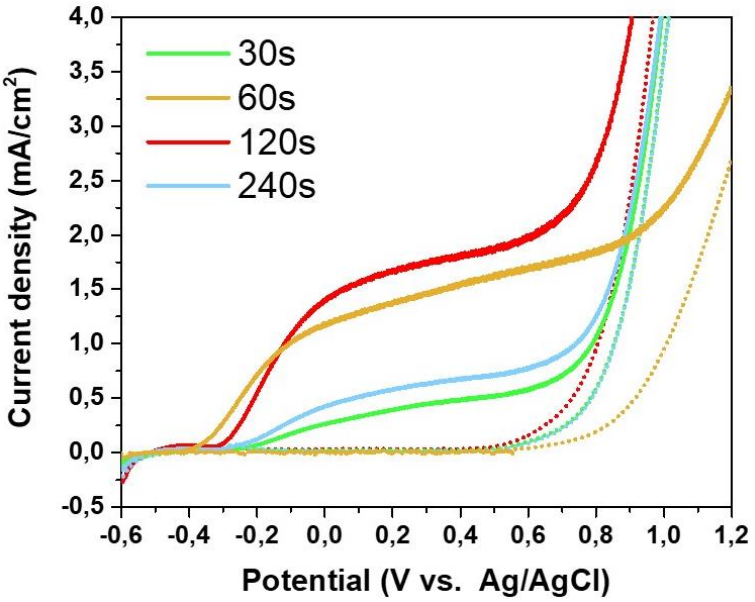

Figure 36 - $BiVO_4$ prepared by different electrodeposition times. Solid lines represent light part of measurement and dotted lines represent dark part of measurements. All four samples were measured in PBS + 0.1M Na_2SO_3.

$BiVO_4$ prepared by conversion from BiOI electrodeposited for 120 s showed the best photoelectrochemical performance and that is why it was further studied and measured in four different electrolytes such as PBS (pH = 7), Na_2SO_3, Na_2SO_4 and in PBS with Na_2SO_3. Figure 37 shows the linear sweep voltammetry scans of the 120 s samples recorded in different electrolytes such as a PBS. The best photocurrent was achieved in 0.5M Na_2SO_3 and then in PBS + Na_2SO_3. The Na_2SO_3 in PBS serves as a hole scavenger that improve photocatalytic performance due to evolving of sulphite radicals which provide great reducing and oxidizing capabilities[104].

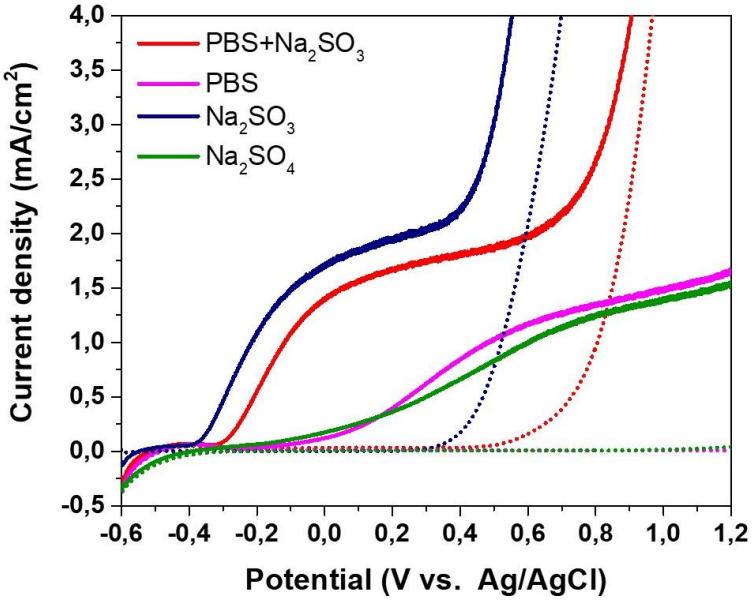

Figure 37 - LSV measurements in four different electrolytes – 0.1M PBS (pH=7), 0.5M Na_2SO_4, 0.5M Na_2SO_3, PBS + 0.1M Na_2SO_3.Solid lines represents light parts of measurement and dotted lines represents dark part of measurement. BiVO4 was made by conversion from BiOI prepared by 120 s of electrodeposition.

These properties were observed also at chronoamperometry (ChAM) measurements (Figure 38) showing the dependency of current density (the photocurrent) on time at constant applied potential of 0.5 V besides the measurement using the Na_2SO_3 electrolyte that had to be performed at the potential of 0.2 V due to the significantly shifted oxygen evolution onset potential as it is clearly seen in Figure 37 . The ChAM measurement shows sufficiently long chemical stability. Moreover, there are only small current density spikes that are commonly caused by fast electron – hole recombination appearing immediately when the light is on[77,105].

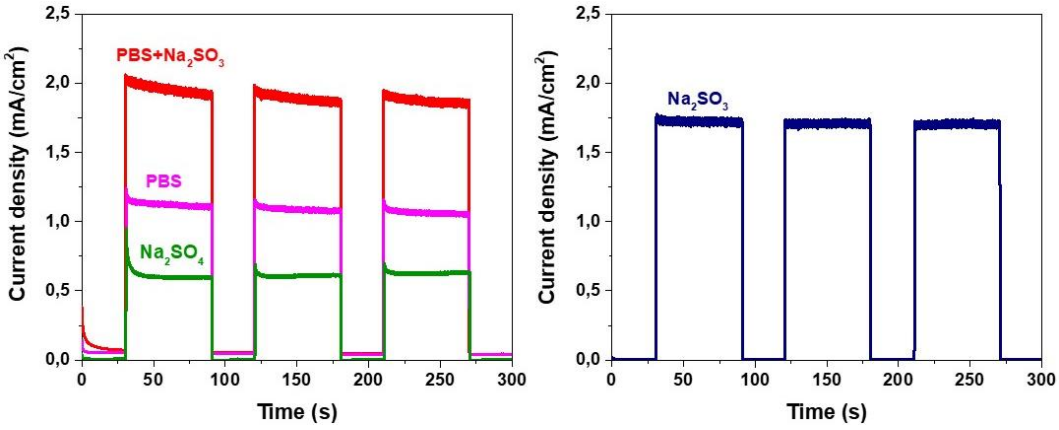

Figure 38- ChAM measurements of BiVO4 in four different electrolytes- PBS (pH=7), 0.5M Na2SO4, 0.5M Na2SO3, PBS + 0.1M Na2SO3. Potential was set at 0.5 V at the right figure and 0.2 V at the right.

The electrochemical impedance spectroscopy (EIS) measurements (Figure 39) confirmed the results obtained from the LSV measurements. The EIS provides information about charge – transfer resistance at the electrode interface under light illumination. The half circle in the Nyquist diagram represent a charge transfer resistance. The smaller diameter of half circle indicate more effective electron – hole separation and thus higher photocurrent[106]. These EIS results are in line with LSV measurements in PBS because at the applied potential 0.3 V the charge transfer is worse than at the potential of 0.5 V (all potentials were measured versus Ag/AgCl electrode) can be seen in Figure 37.

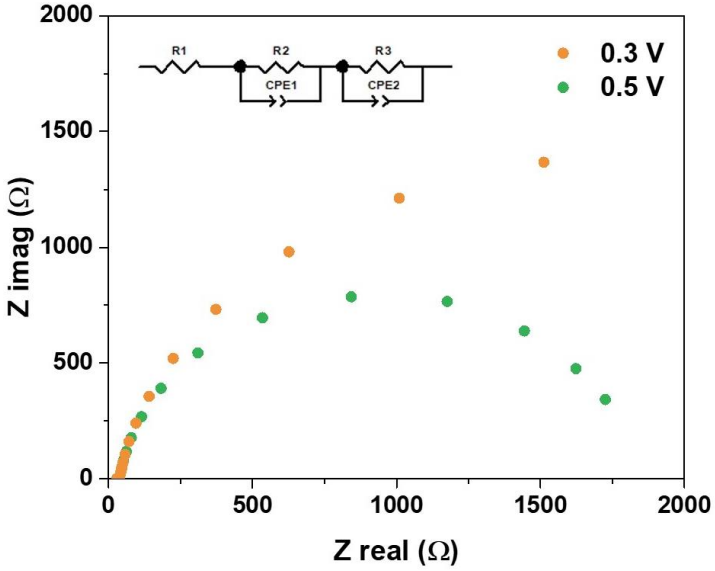

Figure 39 - EIS measurements of $BiVO_4$ in 0.1 M PBS (pH = 7) under illumination at constant potentials 0.3 V and 0.5 V

8.4 $BiVO_4$ doped by molybdenum and tungsten

The doping techniques were used in order to further improve the photoinduced functionality of the $BiVO_4$ films. The elemental doping increases the electrical conductivity, which in turn leads to better charge separation and dynamics, and thus higher photoactivity. Tungsten and molybdenum were chosen as the doping elements due to theirs different valence and similar ionic radius compared to vanadium[83].

The surface SEM images displayed in Figure 40 revealed the final morphology of $BiVO_4$ after doping and secondary annealing. Particles in both cases aggregate together and form bigger particles. $BiVO_4$ doped by Mo changes structure of single particles and particle surface is not anymore sufficiently homogenous than the undoped. Very similar morphology was observed also for the W doped $BiVO_4$ photoelectrodes.

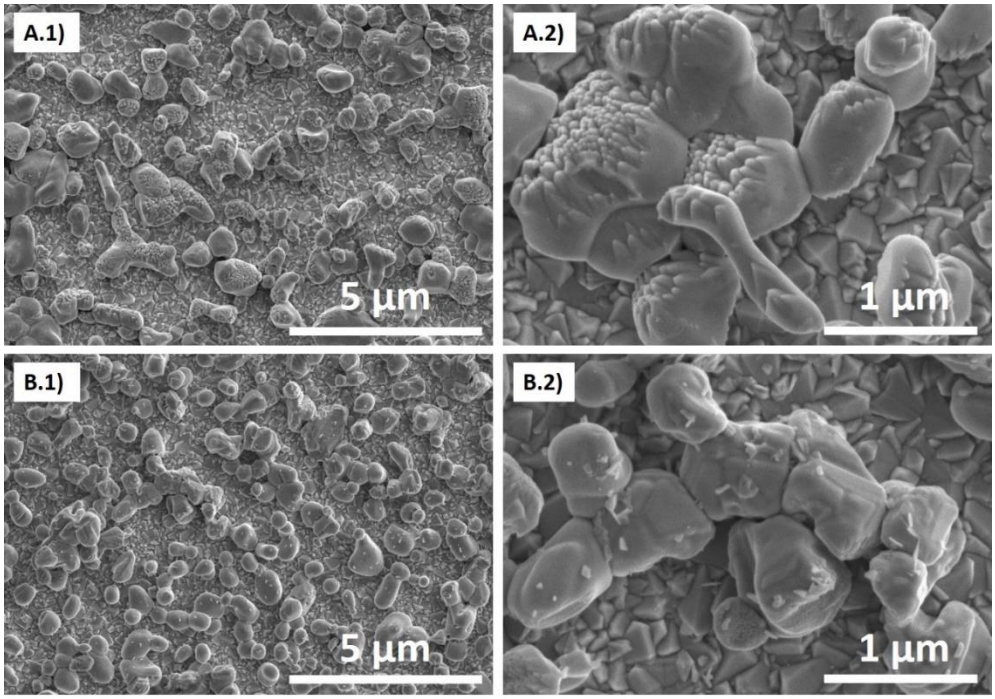

Figure 40 - $BiVO_4$ doped by molybdenum A.1), A.2) and tungsten B.1), B.2)

EDS spectra taken during SEM measurements confirmed the presence of bismuth, vanadium oxygen and also doping elements such as tungsten and molybdenum (Figure 41).

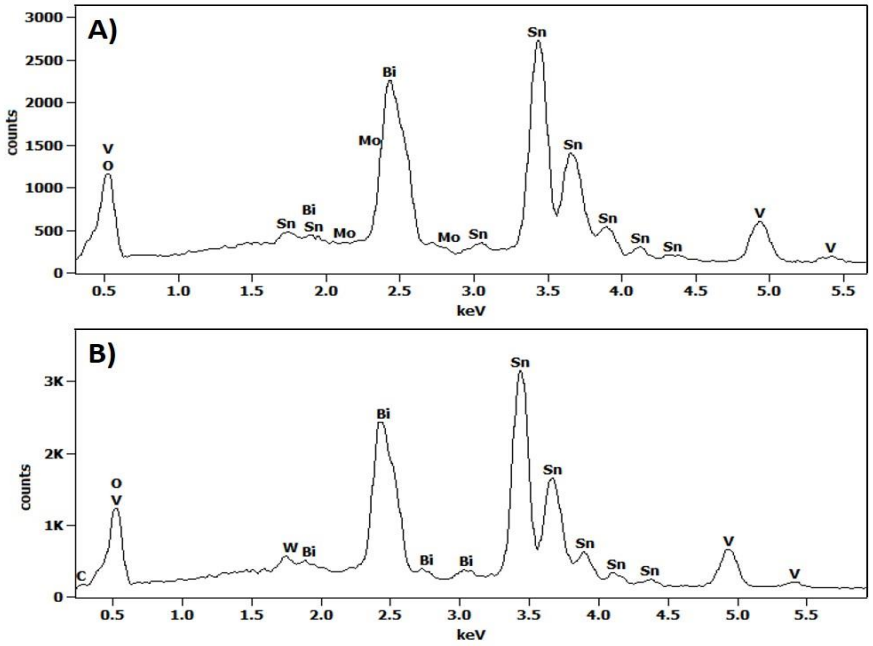

Figure 41 - EDS measurements of $BiVO_4$ doped by A) molybdenum and B) tungsten

To further detect and analyse the Mo and W species in the $BiVO_4$ photoanode, the X-ray photoelectron spectroscopy was used. The survey spectrum of pristine $BiVO_4$ is shown in Figure 42. This spectrum clearly demonstrate existence of Bi and V while high resolution spectra confirm presence of molybdenum and tungsten in $BiVO_4$ doped layers (Figure 43).

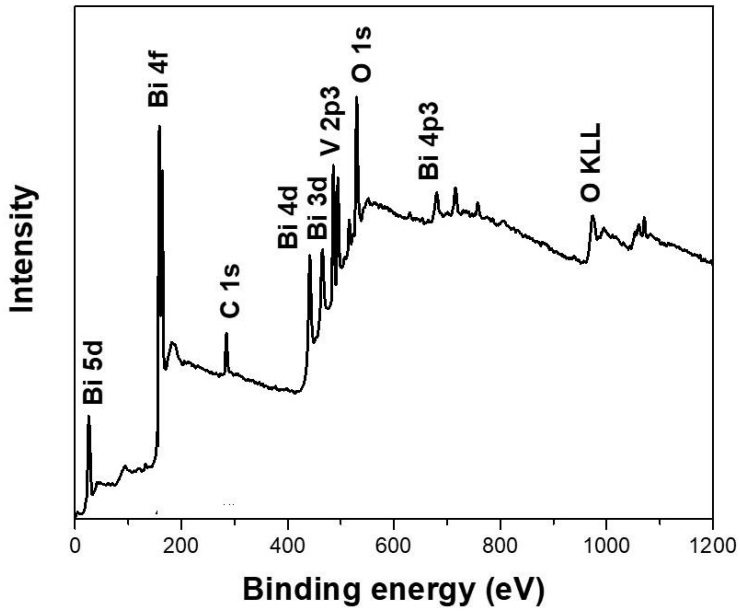

Figure 42 - XPS survey spectra of $BiVO_4$

The binding energy peaks at 158.3 and 163.9 eV are indexed to Bi $4f_{7/2}$ and Bi $4f_{7/2}$ states that are in lines with the result from Bi^{3+}. The peaks at 516 eV are ascribed to V $2p_{3/2}$ states of the VO_4^{3-} tetrahedral. W^{6+} oxidation state in confirmed by biding energy peaks at 35 and 37.1 eV which are assigned to W $4f_{7/2}$ and W $4f_{5/2}$. Trace of Mo^{6+} was detected at binding energies at 232 and 235 eV which are attributed to Mo $3d_{5/2}$ and Mo $3d_{3/2}$. These findings verify that Mo and W were successfully incorporated in the $BiVO_4$ crystal lattice as a Mo^{6+} and W^{6+} and thus serve as the elemental dopants[107].

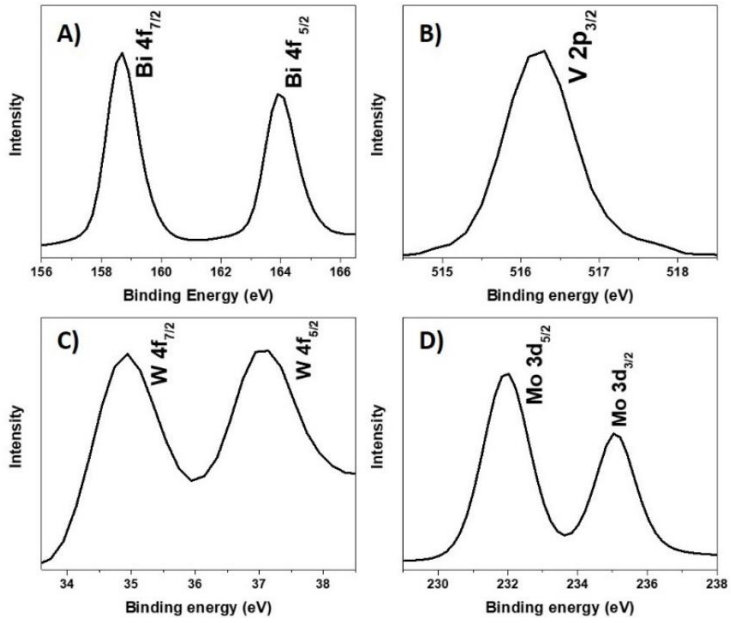

Figure 43 - High resolution XPS spectra. A) bismuth 4f B) vanadium 2p C) tungsten 4f D) molybdenum 3d

Electrochemical impedance spectroscopy further clarifies effect of Mo and W doping (Figure 44). The semi-circular arch diameter of Nyquist plot is related to the charge transfer ability across the semiconductor/electrolyte interface, the one with smaller semi-circular arch has smaller charge transfer resistance, suggests the ability to transfer more charges. Here, the $BiVO_4$ doped by Mo and W showed lower semi-circular arch diameter which indicates higher charger transfer ability than that of pristine $BiVO_4$. Further to extract charge transport/transfer parameters we have fitted the Nyquist plot to an equivalent circuit. The fitting parameters tabulated below (Table 1).

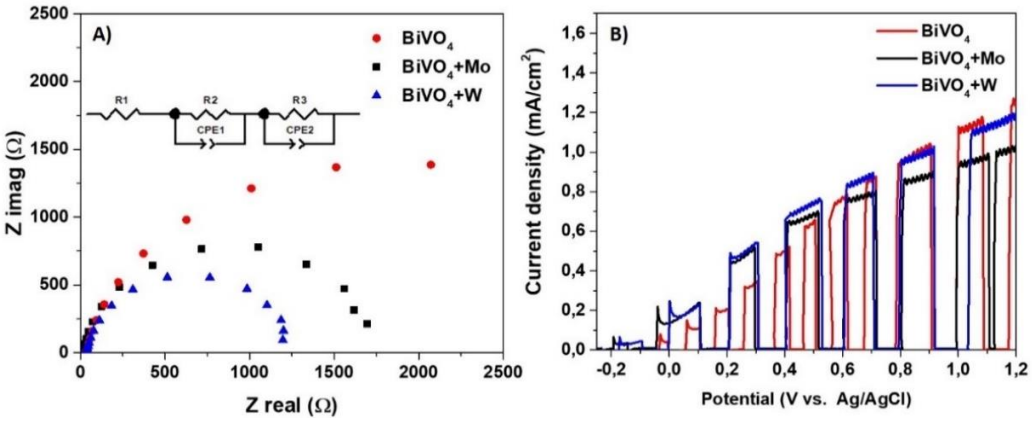

Figure 44 –A) Nyquist diagram of pristine $BiVO_4$ and $BiVO_4$ doped by Mo and W 0.3 V. B) chopped LSV measurement of pristine $BiVO_4$ and $BiVO_4$ doped by Mo and W. Both measurements were proceeded in PBS (pH=7)

From the table, it was observed that the charge transport resistance (Rsc) decreased for $BiVO_4$ + W and $BiVO_4$ + M compared to that of pristine $BiVO_4$. It indicates doping increases the internal conductivity of the material due to creation of internal intermediate energy levels. Further the charger transport resistance (Rct) is also small for doped samples compared to that of pristine $BiVO_4$. It further reveals the more charge transfer to the electrolyte. Capacitance across the semiconductor/electrolyte interface (CSE) is also higher for doped samples, as a result more number of charges will be accumulate at the interface of the semiconductor/electrolyte. This facilitates higher charge transfer ability and in turn enhancement in photocurrent[108].

Table 1 - EIS fitting parameters for pristine $BiVO_4$ and for $BiVO_4$ doped by W and Mo

Sample	Rsc(Ω)	Rct (Ω)	CSE (F)
$BiVO_4$	561	2857	$8.068 \cdot 10^{-5}$
$BiVO_4$ + W	257.1	1155	$11.711 \cdot 10^{-5}$
$BiVO_4$ + M	14.26	1695	$12.498 \cdot 10^{-5}$

9 Conclusion

The presented diploma thesis was focused on photoactive materials with usage for photoelectrochemical water splitting as was mentioned in the aims of diploma thesis. The energy source for this process is sunlight and thus investigated materials must absorb at least a portion of the UV/VIS radiation. All samples were prepared on the most commonly used glass substrate coated by a fluorine doped tin oxide conductive layer (FTO).

The first aim of this diploma thesis was preparation of wide band gap semiconductors such as a titanium dioxide (TiO_2) and tungsten trioxide (WO_3). The TiO_2 prepared by hydrothermal method followed by annealing treatment was the first studied material. The prepared layers had homogenous FTO surface covered by oriented nanorods. It was revealed that the TiO_2 nanorods had a rutile crystalline structure. The TiO_2 nanorod array showed a steady – state plateau photocurrent of 0.5 mA/cm^2 over a relatively wide range of the applied potential (from -0.1 V to 1.1 V vs. Ag/AgCl) when the electrochemical oxygen evolution reaction started to dominate. This rather moderate photoelectrochemical performance was caused due to the narrow range of absorbed radiation.

The second photoactive material was WO_3 prepared similarly as the TiO_2 in the autoclave by hydrothermal method with subsequent annealing process. The surface SEM images of prepared nanostructures showed randomly oriented WO_3 nanorods which were homogenously spread on the surface of FTO. These nanorods appeared in various lengths. The X-ray diffraction revealed the monoclinic crystalline phase of WO_3. Tungsten trioxide provides wider absorption range than TiO_2 but the photoelectrochemical measurements did not performed satisfactory results that reach only 0.6 mA/ cm^2 at the potential of 0.5 V (vs. Ag/AgCl).

According to the aims of diploma thesis, the main objective of this diploma thesis was the $BiVO_4$ photoanode that represented narrow band gap semiconductor. It was prepared by two different methods. The first method based on a drop casting method and with the usage of Triton X-100 surfactant as a structure agent. Different concentrations of Triton X-100 were used. Characterization techniques revealed that this method is not successful due to particle aggregation and poor mechanical stability. Photoelectrochemical performance also did not provide promising results. Thus, another method was sought.

Very perspective method was the two step preparation including electrodeposition of BiOI that serve as a precursor for $BiVO_4$ conversion and subsequent annealing treatment. BiOI was also studied and characterized. It is not interesting from photoelectrochemical point of view due to poor photocurrent results, but it was found that BiOI structure have a major influence on final $BiVO_4$ properties. $BiVO_4$ prepared by conversion from BiOI electrodeposited for 120 s performs almost 2 mA/cm^2 in PBS + 0.1M Na_2SO_3 at 0.5 V vs. Ag/AgCl. Additionally, surface homogeneity and mechanical stability was also satisfactory.

The final aim of this work was the doping of $BiVO_4$ photoanode by molybdenum and tungsten in order to improve $BiVO_4$ photoelectrochemical properties. SEM images revealed structure changes during second annealing where particles aggregate together and form bigger particles compared to pristine $BiVO_4$. Presence of doped elements was confirmed by EDS and also by XPS. Moreover, XPS determined the oxidation states of dopants such as Mo^{6+} and W^{6+}, which means that these elements were incorporated into the crystal lattice of $BiVO_4$. EIS measurements revealed the effect of doping. It was found out that dopants cause decline of intrinsic charge transfer resistance that leads to increasing of internal conductivity and thus to the higher photocurrent density.

All the aims of this diploma thesis were successfully fulfilled. The future research related to the $BiVO_4$ photoanodes can be focused on further study of metal doping techniques that prevent aggregation while maintaining surface homogeneity or using of co-catalysts which can improve surface reactions such as oxygen evolution reaction. Above all, the production of $BiVO_4$ photoanodes on an industrial scale still remains the biggest challenge along with the design and construction of sophisticated systems which will produce hydrogen for fuel cells in economically viable manner that finally provide the green electricity for whole world.

10 Reference

1. Sparrow, P., Brewster, C. & Harris, H. Demographic component of future population growth. *Techinical Pap. No 2013/3* 26 (2013). doi:10.4135/9781452234311.n318

2. Haines, A., Kovats, R. S., Campbell-Lendrum, D. & Corvalan, C. Climate change and human health: Impacts, vulnerability and public health. *Public Health* **120,** 585–596 (2006).

3. Liu, C., Li, F., Ma, L.-P. & Cheng, H.-M. Advanced Materials for Energy Storage. *Adv. Mater.* **22,** E28–E62 (2010).

4. Zuo, W. *et al.* Battery-Supercapacitor Hybrid Devices: Recent Progress and Future Prospects. *Advanced Science* **4,** 1600539 (2017).

5. Goodenough, J. B. & Kim, Y. Challenges for rechargeable Li batteries. *Chemistry of Materials* **22,** 587–603 (2010).

6. Grätzel, M. Photoelectrochemical cells. *Nature* **414,** 338–344 (2001).

7. Yang, L. *et al.* Manipulation of charge transport in ferroelectric-semiconductor hybrid for photoelectrochemical applications. *Nano Energy* **44,** 63–72 (2018).

8. Xu, G. *et al.* Silicon Photoanodes Partially Covered by Ni@Ni(OH)2Core–Shell Particles for Photoelectrochemical Water Oxidation. *ChemSusChem* **10,** 2897–2903 (2017).

9. Kittel, C. *Introduction to solid state physics*. (Wiley, 2005).

10. Walter, M. G. *et al.* Solar water splitting cells. *Chem. Rev.* **110,** 6446–6473 (2010).

11. Nozik, A. J. & Memming, R. Physical Chemistry of Semiconductor−Liquid Interfaces. *J. Phys. Chem.* **100,** 13061–13078 (1996).

12. Brattain, W. H. & Garrett, C. G. B. Experiments on the Interface between Germanium and an Electrolyte. *Bell Syst. Tech. J.* **34,** 129–176 (1955).

13. Licht, S. Multiple band gap semiconductor/electrolyte solar energy conversion. *J. Phys. Chem. B* **105,** 6281–6294 (2001).

14. Gelderman, K., Lee, L. & Donne, S. W. Flat-Band Potential of a Semiconductor: Using the Mott–Schottky Equation. *J. Chem. Educ.* **84,** 685 (2007).

15. Zelitch, I. Improving the efficiency of photosynthesis. *Science* **188,** 626–33 (1975).

16. Qi, J., Zhang, W. & Cao, R. Solar-to-Hydrogen Energy Conversion Based on

Water Splitting. *Adv. Energy Mater.* **8,** 1701620 (2017).

17. Chen, S., Thind, S. S. & Chen, A. Nanostructured materials for water splitting - State of the art and future needs: A mini-review. *Electrochemistry Communications* **63,** 10–17 (2016).

18. Fujishima, A. & Honda, K. Electrochemical photolysis of water at a semiconductor electrode. *Nature* **238,** 37–38 (1972).

19. Liu, H. *et al.* Crystallinity control of TiO 2 hollow shells through resin-protected calcination for enhanced photocatalytic activity. *Energy Environ. Sci.* **8,** 286–296 (2015).

20. Zhao, W., Ma, W., Chen, C., Zhao, J. & Shuai, Z. Efficient Degradation of Toxic Organic Pollutants with Ni 2 O 3 /TiO 2 - x B x under Visible Irradiation. *J. Am. Chem. Soc.* **126,** 4782–4783 (2004).

21. Liu, L., Zhao, H., Andino, J. M. & Li, Y. Photocatalytic CO 2 reduction with H 2O on TiO 2 nanocrystals: Comparison of anatase, rutile, and brookite polymorphs and exploration of surface chemistry. *ACS Catal.* **2,** 1817–1828 (2012).

22. Habisreutinger, S. N., Schmidt-Mende, L. & Stolarczyk, J. K. Photocatalytic reduction of CO2 on TiO2 and other semiconductors. *Angewandte Chemie - International Edition* **52,** 7372–7408 (2013).

23. O'Regan, B. & Grätzel, M. A low-cost, high-efficiency solar cell based on dye-sensitized colloidal TiO2 films. *Nature* **353,** 737–740 (1991).

24. Zhao, J. *et al.* Single crystalline CH3NH3PbI3self-grown on FTO/TiO2substrate for high efficiency perovskite solar cells. *Sci. Bull.* **62,** 1173–1176 (2017).

25. He, X. *et al.* Supercapacitor of TiO2 nanofibers by electrospinning and KOH treatment. *Mater. Des.* **106,** 74–80 (2016).

26. Guler, M. O., Cevher, O., Cetinkaya, T., Tocoglu, U. & Akbulut, H. High capacity TiO2 anode materials for Li-ion batteries. *Energy Convers. Manag.* **72,** 111–116 (2013).

27. Ge, M. *et al.* A review of one-dimensional TiO 2 nanostructured materials for environmental and energy applications. *J. Mater. Chem. A* **4,** 6772–6801 (2016).

28. Muscat, J., Swamy, V. & Harrison, N. M. First-principles calculations of the phase stability of TiO 2. *Phys. Rev. B* **65,** 224112 (2002).

29. Yang, Z. *et al.* Synthesis of Crystal-Controlled TiO2Nanorods by a Hydrothermal Method: Rutile and Brookite as Highly Active Photocatalysts. *J. Phys. Chem. C* **119,** 16905–16912 (2015).

30. Alsawat, M., Altalhi, T., Shapter, J. G. & Losic, D. Influence of dimensions, inter-distance and crystallinity of titania nanotubes (TNTs) on their photocatalytic activity. *Catal. Sci. Technol.* **4,** 2091 (2014).

31. Haggerty, J. E. S. *et al.* High-fraction brookite films from amorphous precursors. *Sci. Rep.* **7,** 15232 (2017).

32. Mi, Y. & Weng, Y. Band Alignment and Controllable Electron Migration between Rutile and Anatase TiO<inf>2</inf>. *Sci. Rep.* **5,** 11482 (2015).

33. T. Sumita, T. Yamaki, S. Yamamoto & A. Miyashita. Photo-induced surface charge separation of highly oriented TiO2 anatase and rutile thin ®lms. *Appl. Surf. Sci.* **200,** 21 (2002).

34. Guimarães, R. R., Parussulo, A. L. A., Toma, H. E. & Araki, K. Enlightening the synergic effect of anatase/rutile mixtures in solar cells. *Electrochim. Acta* **188,** 523–528 (2016).

35. Chao, J.-J., Wang, J.-J., Shiu, S.-C., Hung, S.-C. & Lin, C.-F. Hydrothermal Synthesis of TiO2 Nanorod Arrays on Transparent Conducting Substrates. *2011 11th IEEE Int. Conf. Nanotechnol.* 1235–1238 (2011). doi:10.1109/NANO.2011.6144576

36. Zhang, D. R., Cha, H. G. & Kang, Y. S. Hydrothermal Synthesis of Anatase TiO2 Nanorods with High Crystallinity Using Ammonia Solution as a Solvent. *J. Nanosci. Nanotechnol.* **11,** 6007–6012 (2011).

37. Kathirvel, S. *et al.* Solvothermal synthesis of TiO2nanorods to enhance photovoltaic performance of dye-sensitized solar cells. *Sol. Energy* **132,** 310–320 (2016).

38. Ramakrishnan, V. M., Natarajan, M., Santhanam, A., Asokan, V. & Velauthapillai, D. Size controlled synthesis of TiO2 nanoparticles by modified solvothermal method towards effective photo catalytic and photovoltaic applications. *Mater. Res. Bull.* **97,** 351–360 (2018).

39. Sulka, G. D., Kapusta-Kołodziej, J., Brzózka, A. & Jaskuła, M. Fabrication of nanoporous TiO2 by electrochemical anodization. *Electrochim. Acta* **55,** 4359–4367 (2010).

40. Maruyama, T. & Arai, S. Titanium dioxide thin films prepared by chemical vapor deposition. *Sol. Energy Mater. Sol. Cells* **26,** 323–329 (1992).

41. Doh, S. J., Kim, C., Lee, S. G., Lee, S. J. & Kim, H. Development of photocatalytic TiO2 nanofibers by electrospinning and its application to degradation of dye pollutants. *J. Hazard. Mater.* **154,** 118–127 (2008).

42. Zheng, J., Bao, S., Guo, Y. & Jin, P. TiO2 films prepared by DC reactive

magnetron sputtering at room temperature: Phase control and photocatalytic properties. *Surf. Coatings Technol.* **240,** 293–300 (2014).

43. Yang, H., Zhu, S. & Pan, N. Studying the mechanisms of titanium dioxide as ultraviolet-blocking additive for films and fabrics by an improved scheme. *J. Appl. Polym. Sci.* **92,** 3201–3210 (2004).

44. Matsumoto, Y., Kurimoto, J., Shimizu, T. & Sato, E. Photoelectrochemical Properties of Polycrystalline TiO[sub 2] Doped with 3d Transition Metals. *J. Electrochem. Soc.* **128,** 1040 (1981).

45. Tiwari, A., Mondal, I., Ghosh, S., Chattopadhyay, N. & Pal, U. Fabrication of mixed phase TiO 2 heterojunction nanorods and their enhanced photoactivities. *Phys. Chem. Chem. Phys.* **18,** 15260–15268 (2016).

46. Zhang, W. *et al.* TiO2nanorods: A facile size- and shape-tunable synthesis and effective improvement of charge collection kinetics for dye-sensitized solar cells. *ACS Appl. Mater. Interfaces* **6,** 9698–9704 (2014).

47. Pu, Y. C. *et al.* Au nanostructure-decorated TiO2nanowires exhibiting photoactivity across entire UV-visible region for photoelectrochemical water splitting. *Nano Lett.* **13,** 3817–3823 (2013).

48. Butler, M. A., Nasby, R. D. & Quinn, R. K. Tungsten trioxide as an electrode for photoelectrolysis of water. *Solid State Commun.* **19,** 1011–1014 (1976).

49. Zheng, H., Tachibana, Y. & Kalantar-Zadeh, K. Dye-sensitized solar cells based on WO3. *Langmuir* **26,** 19148–19152 (2010).

50. Logie, V., Wehrer, P., Katrib, A. & Maire, G. Catalytic activity of bulk WO3for the reforming of hexanes and hexenes. *J. Catal.* **189,** 438–448 (2000).

51. Palnichenko, A. V., Vyaselev, O. M., Mazilkin, A. A., Zver'kova, I. I. & Khasanov, S. S. Metastable superconductivity of W/WO3 interface. *Phys. C Supercond. its Appl.* **534,** 61–67 (2017).

52. Szilágyi, I. M. *et al.* WO3photocatalysts: Influence of structure and composition. *J. Catal.* **294,** 119–127 (2012).

53. Kalanur, S. S., Hwang, Y. J., Chae, S. Y. & Joo, O. S. Facile growth of aligned WO3 nanorods on FTO substrate for enhanced photoanodic water oxidation activity. *J. Mater. Chem. A* **1,** 3479 (2013).

54. Ofori, Frank Agyemang. Sheikh, Faheem A. Appiah-Ntiamoah, Richard. Yang, Xinsheng. Kim, H. A Simple Method of Electrospun Tungsten Trioxide Nanofibers with Enhanced Visible-Light Photocatalytic Activity. *Nano-Micro Lett.* **7,** 291–297 (2015).

55. Chen, X. *et al.* Ultrathin, single-crystal WO3nanosheets by two-dimensional oriented attachment toward enhanced photocatalystic reduction of CO2into hydrocarbon fuels under visible light. *ACS Appl. Mater. Interfaces* **4,** 3372–3377 (2012).

56. Sadakane, M. *et al.* Preparation of 3-D ordered macroporous tungsten oxides and nano-crystalline particulate tungsten oxides using a colloidal crystal template method, and their structural characterization and application as photocatalysts under visible light irradiation. *J. Mater. Chem.* **20,** 1811 (2010).

57. Bauersfeld, M. L., Neumaiera, P. & Wöllenstein, J. Nanoporous tungsten trioxide grown by electrochemical anodization of tungsten for gas sensing applications. in *Procedia Engineering* **47,** 204–207 (Elsevier, 2012).

58. Lee, K. D. Deposition of WO3 thin films by the sol-gel method. *Coating* **302,** 84–88 (1997).

59. Huirache-Acuña, R., Paraguay-Delgado, F., Albiter, M. A., Lara-Romero, J. & Martínez-Sánchez, R. Synthesis and characterization of WO3nanostructures prepared by an aged-hydrothermal method. *Mater. Charact.* **60,** 932–937 (2009).

60. An, X. *et al.* WO3 nanorods/graphene nanocomposites for high-efficiency visible-light-driven photocatalysis and NO2 gas sensing. *J. Mater. Chem.* **22,** 8525 (2012).

61. Guo, J. *et al.* Synthesis of WO 3 @Graphene composite for enhanced photocatalytic oxygen evolution from water. *RSC Adv.* **2,** 1356–1363 (2012).

62. Xiang, Q. *et al.* Au Nanoparticle Modified WO 3 Nanorods with Their Enhanced Properties for Photocatalysis and Gas Sensing. *J. Phys. Chem. C* **114,** 2049–2055 (2010).

63. Xiang, Q. *et al.* Au nanoparticle modified WO3 nanorods with their enhanced properties for photocatalysis and gas sensing. *J. Phys. Chem. C* **114,** 2049–2055 (2010).

64. Roru, R. S. & Wenrnc, J. L. SYNTHESIS AND STABILITY OF BISMUTOTANTALI'I'E, STIBIOTANTALITE AND CHEMICALLY SIMILAR ABO4 COMPOUNDS. *TTIE Am. Mineral.* **18,** (1963).

65. Kudo, A., Ueda, K., Kato, H. & Mikami, I. Photocatalytic O2 evolution under visible light irradiation on BiVO4 in aqueous AgNO3 solution. *Catal. Letters* **53,** 229–230 (1998).

66. Kudo, A., Omori, K. & Kato, H. A novel aqueous process for preparation of crystal form-controlled and highly crystalline BiVO4 powder from layered vanadates at room temperature and its photocatalytic and photophysical properties. *J. Am. Chem. Soc.* **121,** 11459–11467 (1999).

67. Patil, S. S. *et al.* One-pot in situ hydrothermal growth of BiVO4/Ag/rGO hybrid architectures for solar water splitting and environmental remediation. *Sci. Rep.* **7,** (2017).

68. Prévot, M. S. & Sivula, K. Photoelectrochemical Tandem Cells for Solar Water Splitting. *J. Phys. Chem. C* **117,** 17879–17893 (2013).

69. Tolod, K., Hernández, S. & Russo, N. Recent Advances in the BiVO4 Photocatalyst for Sun-Driven Water Oxidation: Top-Performing Photoanodes and Scale-Up Challenges. *Catalysts* **7,** 13 (2017).

70. Tokunaga, S., Kato, H. & Kudo, A. Selective preparation of monoclinic and tetragonal BiVO4 with scheelite structure and their photocatalytic properties. *Chem. Mater.* **13,** 4624–4628 (2001).

71. F David, W. I. Ferroelastic phase transition in BiVO4 : III. Thermodynamics Ferroelastic phase transition in BiVO,: 111. Thermodynamics. *J. Phys. C J. Phys. C Solid State Phys* **16,** 5093–5118 (1983).

72. Walsh, A., Yan, Y., Huda, M. N., Al-Jassim, M. M. & Wei, S. H. Band edge electronic structure of BiVO 4: Elucidating the role of the Bi s and V d orbitals. *Chem. Mater.* **21,** 547–551 (2009).

73. Hernández, S., Gerardi, G., Bejtka, K., Fina, A. & Russo, N. Evaluation of the charge transfer kinetics of spin-coated BiVO4 thin films for sun-driven water photoelectrolysis. *Appl. Catal. B Environ.* **190,** 66–74 (2016).

74. He, H. *et al.* Synthesis of BiVO 4 nanoflake array films for photoelectrochemical water oxidation. *J. Mater. Chem. A* **2,** 9371–9379 (2014).

75. Abdi, F. F. & Van De Krol, R. Nature and light dependence of bulk recombination in Co-Pi-catalyzed BiVO 4 photoanodes. *J. Phys. Chem. C* **116,** 9398–9404 (2012).

76. Myung, N. *et al.* Tailoring Interfaces for Electrochemical Synthesis of Semiconductor Films: $BiVO_4$, Bi_2O_3 , or Composites. *J. Phys. Chem. C* **115,** 7793–7800 (2011).

77. Zachäus, C., Abdi, F. F., Peter, L. M. & van de Krol, R. Photocurrent of BiVO 4 is limited by surface recombination, not surface catalysis. *Chem. Sci.* **8,** 3712–3719 (2017).

78. Ressnig, D., Kontic, R. & Patzke, G. R. Morphology control of BiVO4 photocatalysts: pH optimization vs. self-organization. *Mater. Chem. Phys.* **135,** 457–466 (2012).

79. Su, J., Guo, L., Bao, N. & Grimes, C. A. Nanostructured WO_3 /$BiVO_4$ Heterojunction Films for Efficient Photoelectrochemical Water Splitting. *Nano*

Lett. **11,** 1928–1933 (2011).

80. Zhang, B. *et al.* Doping strategy to promote the charge separation in BiVO4 photoanodes. *Appl. Catal. B Environ.* **211,** 258–265 (2017).

81. Iwase, A., Nozawa, S., Adachi, S. & Kudo, A. Preparation of Mo- and W-doped BiVO4 fine particles prepared by an aqueous route for photocatalytic and photoelectrochemical O2 evolution. *J. Photochem. Photobiol. A Chem.* **353,** 284–291 (2018).

82. Monfort, O. *et al.* Comparative study between pristine and Nb-modified BiVO4 films employed for photoelectrocatalytic production of H2 by water splitting and for photocatalytic degradation of organic pollutants under simulated solar light. *Catal. Today* **280,** 51–57 (2017).

83. Zhao, X. & Chen, Z. Enhanced photoelectrochemical water splitting performance using morphology-controlled BiVO 4 with W doping. *Beilstein J. Nanotechnol.* **8,** 2640–2647 (2017).

84. Atkins, P. & De Paula, J. *Fyzikální chemie*. (Vysoká škola chemicko technologická, 2013).

85. Bunaciu, A. A., Udriştioiu, E. gabriela & Aboul-Enein, H. Y. X-Ray Diffraction: Instrumentation and Applications. *Critical Reviews in Analytical Chemistry* **45,** 289–299 (2015).

86. Curry, T. S., Dawdey, J. E., Murry, R. C. *Christensens's Physics of Diagnostic Radiology*. (Lea & Febiger, 1990). doi:radiology.180.3.766

87. Biesinger, M. C., Lau, L. W. M., Gerson, A. R. & Smart, R. S. C. Resolving surface chemical states in XPS analysis of first row transition metals, oxides and hydroxides: Sc, Ti, V, Cu and Zn. *Appl. Surf. Sci.* **257,** 887–898 (2010).

88. Deville, J.-P. La spectroscopie des électrons Auger. *Rev. Phys. Appliquée* **3,** 351–355 (1968).

89. Rodríguez-Carvajal, J. Recent advances in magnetic structure determination by neutron powder diffraction. *Phys. B Phys. Condens. Matter* **192,** 55–69 (1993).

90. Abbe, E. Beiträge zur theorie des mikroskops und der mikroskopischen wahrnehmung. *Arch. Mikros. Anat.* **9,** (1873).

91. Kubínek, R., Šafářová, K. & Vůjtek, M. *Elektronová mikroskopie*. (Univerzita Palackého v Olomouci, 2011).

92. Scanning Electron Microscopes (SEM) | Introduction to JEOL Products | JEOL Ltd. Available at: https://www.jeol.co.jp/en/science/sem.html. (Accessed: 12th April 2018)

93. Němcová, I., Čermáková, L. & Rychlovský, P. *Spektrometrické analytické metody*. (Karolinum, 1997).

94. RAMAN, C. V. & KRISHNAN, K. S. A New Type of Secondary Radiation. *Nature* **121,** 501–502 (1928).

95. Long, D. A. Introductory Raman Spectroscopy. John R. Ferraro, Kazuo Nakamoto and Chris W. Brown. Academic Press, Amsterdam, Second Edition, 2003. xiii + 434. *J. Raman Spectrosc.* **36,** 1012–1012 (2005).

96. McDonald, K. J. & Choi, K.-S. A new electrochemical synthesis route for a BiOI electrode and its conversion to a highly efficient porous BiVO4 photoanode for solar water oxidation. *Energy Environ. Sci.* **5,** 8553 (2012).

97. Gamry Instruments. Basics of EIS: Electrochemical Research-Impedance. (2016). Available at: https://www.gamry.com/application-notes/EIS/basics-of-electrochemical-impedance-spectroscopy/. (Accessed: 23rd April 2018)

98. Chen, J., Tao, H. B. & Liu, B. Unraveling the Intrinsic Structures that Influence the Transport of Charges in TiO2 Electrodes. *Advanced Energy Materials* **7,** 1700886 (2017).

99. Lopes, O. F. *et al.* Synthesis of BiVO 4 via oxidant peroxo-method: insights into the photocatalytic performance and degradation mechanism of pollutants. *New J. Chem.* **39,** 6231–6237 (2015).

100. Yu, J. & Kudo, A. Effects of Structural Variation on the Photocatalytic Performance of Hydrothermally Synthesized BiVO4. *Adv. Funct. Mater.* **16,** 2163–2169 (2006).

101. Frost, R. L., Henry, D. A., Weier, M. L. & Martens, W. Raman spectroscopy of three polymorphs of BiVO4: clinobisvanite, dreyerite and pucherite, with comparisons to (VO4)3-bearing minerals: namibite, pottsite and schumacherite. *J. Raman Spectrosc.* **37,** 722–732 (2006).

102. Luo, W. *et al.* Solar hydrogen generation from seawater with a modified BiVO4 photoanode. *Energy Environ. Sci.* **4,** 4046 (2011).

103. Li, C. *et al.* Monoclinic porous BiVO4networks decorated by discrete g-C3N4nano-islands with tunable coverage for highly efficient photocatalysis. *Small* **10,** 2783–2790 (2014).

104. Deng, W. *et al.* Visible-Light-Driven Photocatalytic Degradation of Organic Water Pollutants Promoted by Sulfite Addition. *Environ. Sci. Technol.* **51,** 13372–13379 (2017).

105. Trzciński, K., Szkoda, M., Sawczak, M., Karczewski, J. & Lisowska-Oleksiak, A. Visible light activity of pulsed layer deposited BiVO4/MnO2films decorated with

gold nanoparticles: The evidence for hydroxyl radicals formation. *Appl. Surf. Sci.* **385,** 199–208 (2016).

106. Kim, K., Kim, M.-J., Kim, S.-I. & Jang, J.-H. Towards Visible Light Hydrogen Generation: Quantum Dot-Sensitization via Efficient Light Harvesting of Hybrid-TiO2. *Sci. Rep.* **3,** 3330 (2013).

107. Zeng, Q. *et al.* Synthesis of WO3/BiVO4photoanode using a reaction of bismuth nitrate with peroxovanadate on WO3film for efficient photoelectrocatalytic water splitting and organic pollutant degradation. *Appl. Catal. B Environ.* **217,** 21–29 (2017).

108. Rambabu, Y., Jaiswal, M. & Roy, S. C. Enhanced photoelectrochemical performance of multi-leg TiO2nanotubes through efficient light harvesting. *J. Phys. D. Appl. Phys.* **48,** 295302 (2015).